

Multi-objective performance optimization of a hydro-static transmission with NSGA-II

Ivan Okhotnikov

May 24, 2021

This research presents implementation of multi-objective optimization to resolve the conflicting requirements in design of high-power hydro-static transmissions made of a variable axial piston pump and a fixed axial piston motor. The goal is to identify and to investigate the Pareto optimal combinations of a pump maximum displacement, its shaft speed and the pressure differential in the closed circuit of the variable displacement hydro-static transmission. Such combinations form the Pareto optimal front of the total efficiency, transmitted power and the total weight of the transmission subject to the pump speed constraint. The efficiency objective model was constructed as a product of the developed analytical volumetric efficiency and the empirical mechanical efficiency, both dependant on the displacement. The validation of the analytical volumetric efficiency model through measurements and analysis of the transmission speed ratio on a large sample of transmissions is presented and discussed. The total linear mass objective and exponential pump speed constraint models were built according to the collected manufacturers catalogues data for axial piston machines and data regression analysis. The regression models were five-fold cross-validated resulting in high accuracy and determination. The Pareto-optimal set of variables and front of objectives were obtained with the non-dominated sorting genetic algorithm, NSGA-II. Objectives convergence to the optimum was established. The distributions and relative densities of the Pareto optimal solutions within the feasible search space were analysed. The optimal solutions tend to accumulate along the boundaries and constraints of the design variables gravitating towards the high pressures region. In the Pareto front for the clearances invariant transmissions, the negative correlation was observed between the transmitted power and the total efficiency.

Nomenclature

Latin

a_1, a_2, a_3	Coefficients in the exponential speed constraint model
A_*	Coefficient in the mechanical efficiency model

b_1, b_2, b_3, b_4	Constraint coefficients in the mass objective model
B_*	Coefficient in the mechanical efficiency model
d	Piston diameter, mm
D_*	Coefficient in the mechanical efficiency model
D	Pitch circle diameter, mm
e	Piston eccentricity, μm
f_m	m -th objective function
\mathbf{f}	Vector objective function
\mathcal{F}	Feasible search or design space
g_j	j -th constraint function
h	Piston stroke, mm
h_k	k -th constraint function
h_1, h_2, h_3	Clearances of the leakage paths, μm
i, I	Index and the number of decision variables
j, J	Index and the number of inequality constraints
k, K	Index and the number of equality constraints
k_1, \dots, k_5	Design balances
l	Length, mm
m, M	Mass, kg; index and the number of objective functions
n	Angular speed, rpm
N	Population size
\mathbb{N}	Set of natural numbers
\mathcal{O}	Objective space
p	Pressure, bar
P	Power, kW
Q	Volume flow rate, lpm
r	Minor radius, mm
R	Major radius, mm,
\mathbb{R}	Set of real numbers
\mathcal{S}	Search or design space
t	Block land width, mm
T	Torque, N m
V	Volumetric displacement, cc/rev
w	Kidney width, mm
x_i	i -th variable

\mathbf{x}	Decision or solution vector
y_m	m -th objective, an image of the m -th objective function f_m
\mathbf{y}	Objective vector corresponding to $\mathbf{f}(\mathbf{x})$
z	Number of pistons

Greek

β	Oil bulk modulus, GPa
σ	Standard deviation
γ	Swash angle, $^\circ$
η	Efficiency, %
μ	Oil dynamic viscosity, Pa s; mean value

Acronyms

APM	Axial Piston Machine
BDC	Bottom Dead Centre
EHA	Electro-Hydraulic Actuator
HST	Hydro-Static Transmission
KDE	Kernel Density Estimation
MO	Multi-Objective
PCD	Pitch Circle Diameter
RMSE	Root mean square error
SD	Standard Deviation
TDC	Top Dead Centre

Subscripts

$*$	All elements in a row or a column
bi	Block inner
bo	Block outer
e	Engagement
gen	Generations
h	High
$hydr$	Hydraulic
HST	Hydro-static transmission
HST_m	Hydro-static transmission, mechanical
HST_v	Hydro-static transmission, volumetric
in	Input
l	Low
L	Leakage

m	Mass
mm	Motor mass
mp	Pump mass
M	Motor
Mm	Motor mechanical
Mv	Motor volumetric
nm	Motor speed
np	Pump speed
out	Output
p	Piston, Pareto
P	Pump
$P.lim$	Pump limiting
Pm	Pump mechanical
Pv	Pump volumetric
s	Slipper, speed
th	Theoretical
Superscripts	
G	Global
L	Lower
U	Upper
x	Non-dominated position
y	Non-dominated objective

1 Introduction

Finding a reasonable balance between conflicting weight, efficiency and transmitted power requirements is a common challenge in the specification definition and setting targets for the conceptual design of high-power hydraulic systems. Poorly selected rated operating conditions would deteriorate system performance, may result in over- or under designed structural components, may even cause catastrophic failures. Project-wise wrong nominal operating conditions could cause creeping specification Ullman [2009]. Astounding developments in a field of optimization led engineers to recognize optimization algorithms as a powerful tool to find a tradeoff between contradicting requirements. In aerospace, solutions of multi-objective (MO) optimization problems has become a standard practice Arias-Montano et al. [2012].

Electro-hydraulic actuators (EHA) have become a notable application area of MO optimization.

12 The optimization approach has been proposed for a preliminary design of the EHA driving aircraft
13 control surfaces in Wu et al. [2017], where the EHA weight and efficiency were optimized relative to
14 the lever length, pump displacement and electric motor torque constant. Since the weight objective
15 function, and the operational speed constraint are notoriously difficult to derive analytically through
16 the pump displacement, the empirical data from available manufacturers catalogues and curve fitting
17 were used.

18 Although this scaling-law approach provides functions that are relatively easy to operate with
19 mathematically, in order to obtain an accurate model a large number of products from different
20 manufacturers in a wide specifications range is required. Despite this drawback, the empirical way
21 to predict objective functions has been employed throughout the mechanical engineering field for a
22 number of years Fraj et al. [2012], Liscouët et al. [2011], Budinger et al. [2012, 2014].

23 MO optimization research in engineering is often accompanied with further investigation of
24 the optimal solutions as a form of a decision making strategy. Thus, the research work on EHA
25 optimization has been extended further by modelling and analyzing dynamic performance of optimal
26 solutions Yu et al. [2018]. The particle swarm optimization method Coello and Lechuga [2002] was
27 applied to find the Pareto boundary in this study. However, the global optimum was obtained from
28 the Pareto front through the analytic hierarchy process.

29 The weight and efficiency objectives have been complemented with the dynamics criteria of the
30 rise time and stiffness in Xue et al. [2019]. Fast and stable dynamics of the hydro-mechanical systems
31 is imperative in a vehicle transmission operation due to requirements to response times, damping and
32 resonance Larsson [2019]. The research has proposed the holistic simulation driven design method
33 implementing script based generation of design parameters and loads with subsequent transfer to
34 and dynamic simulation within the AMESim environment. It is claimed that the approach has
35 allowed authors to shorten time needed to evaluate objectives across the range of possible motion
36 and load demands. The AMESim coupled optimization was also used in the preliminary design of
37 the EHA of the launch vehicle application, where the optimization objectives were mass, efficiency
38 and bandwidth Zhang et al. [2020].

39 MO optimization proved to be useful for a component level improvements as well. A remarkable
40 example is application of the non-dominated sorting genetic algorithm (NSGA-II) to optimize a
41 shape of micro dimples on a valve plate in order to minimize mechanical and volumetric losses
42 occurring in the cylinder block/valve plate interface of an axial piston pump in an EHA Chen et al.
43 [2019]. Component level optimization demonstrated efficacy in enhancing dynamic properties as
44 well as stability of pressure control valves in vehicle automatic transmission Jian et al. [2018]. An
45 optimized valve design in this study has shown superior performance in experimental environment,
46 confirming applicability of both the novel simulation model as well as the optimization technique.

47 The highly constrained, multi-domain MO optimization problem was addressed in development

48 of hybrid hydraulic power transmission in a vehicles propulsion system. The adaptive simulated
49 annealing genetic algorithm was employed to optimize the fitness function composed of the
50 braking energy regeneration ability, acceleration time, fuel consumption and added price Hui
51 [2010]. Reduction in fuel consumption and controller induced velocity deviation were analyzed
52 according to the stochastic Complex-RF method with nine design variables Baer et al. [2018], Krus
53 et al. [2003], Box [1965].

54 There have been attempts made to optimize various hydro-static transmission (HST) performance
55 metrics in power split continuously variable hydro-mechanical transmissions of work vehicles. The
56 HST optimization problem has not received the same level of attention as aircraft applications had.
57 Although the demand for large capacity HSTs has been increasing in the recent years Sasaki et al.
58 [2014]. Popularity of HST is mainly due to the ease of control of speed, torque, direction of rotation
59 and safety of operation Korn [1969], and a potential to results in a less fuel consuming powertrain
60 Rossetti and Macor [2018], Macor and Rossetti [2013].

61 The notable examples of HST optimization are the works of Macor and Rosetti Macor and
62 Rossetti [2011], Rossetti and Macor [2013], which have defined the design of a HST as an optimization
63 problem. The optimization approach, thorough analysis of the Pareto fronts derived with swarm
64 methods followed by the test case study helped to establish comparative advantages and limitations
65 of input and output coupled power split layouts. Applying the graph theory to model possible
66 transmission configurations allowed to identify the optimal linkage between epicycles and final
67 drives Rossetti et al. [2017]. The trend to combine optimization with other design methods has
68 been developed further in a proposal of the automated design of hydro-mechanical transmissions
69 Pettersson [2013]. The suggestion to include the optimization methods into the conceptual design
70 was put forward later in Uebel [2017].

71 The current research demonstrates how MO optimization can be applied for the high-power,
72 heavy duty HST in vehicle transmission to find tradeoffs between conflicting requirements of weight,
73 efficiency and transmitted power. This research adopts the detailed analytical approach to construct
74 a mathematical model to predict the HST efficiency as the primary optimization objective, presents
75 the efficiency model validation, develops the exponential empirical constraint model of the pump
76 speed and analyses the MO optimization outcomes in the form of the Pareto-optimal set and
77 front. Based on these, the patterns and mutual relations between the objectives were observed and
78 discussed. The applied method belongs to the evolutionary computation family of algorithms, which
79 are increasingly being used in engineering optimization problems Zhou et al. [2011].

80 2 Hydro-static transmission

2.1 HST operation

A schematic of a typical closed circuit HST system is shown in fig. 1. It serves to continuously transmit the input power P_{in} from a positive displacement variable pump 1 to a fixed displacement motor 8 through oil in high- and low-pressure lines. The mechanical power P_{in} comes to the pump 1 from a prime mover, which normally is internal combustion engine rigidly connected to the HST through a gear train. The input mechanical energy of the rotating pump shaft is being converted into oil flow energy. The pressurized oil, which leaves the pump at high discharge pressure p_h with a flow rate Q_{out} , then comes to the motor 8, where the oil energy is converted back into rotational mechanical energy Korn [1969]. The HST output power P_{out} from the rotating motor shaft is being transmitted further downstream the drivetrain to the final drives of the transmission, which are usually the vehicle wheels or tracks. The oil leaving the motor returns back to the pump. Therefore, the pump 1 is the power input to the HST, the motor 8 – its power output. In fig. 1 and further throughout this research, uppercase subscripts “P” and “M” of any quantity refer to pump and motor sides of the HST respectively.

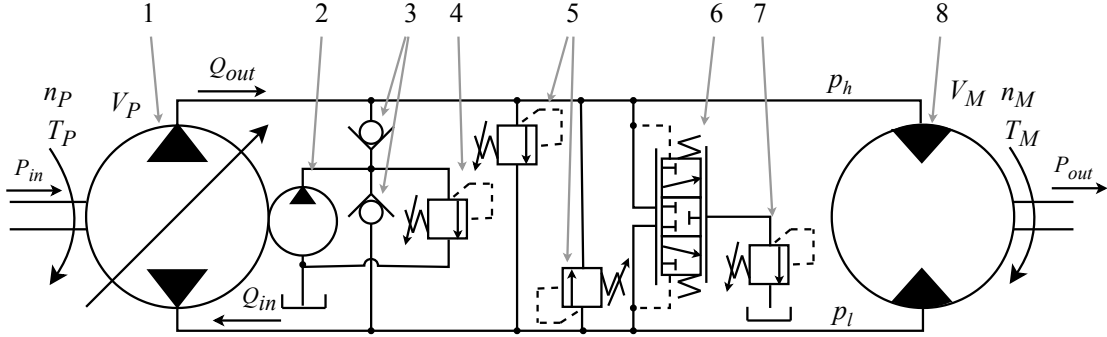


Figure 1: Hydraulic circuit of a typical HST

Since the variable pump 1 has an infinitely adjustable displacement V_P in the range $[-V_{P,max}, V_{P,max}]$, it sends the continuously variable flow rate Q_{out} to the motor dependant on the current pump displacement V_P proportional to the pump swash angle γ . The motor 8 converts the oil flow to the HST output (or motor) speed n_M corresponding to the flow rate Q_{out} entering the motor. Moreover, the HST enables reverse rotation of the HST output shaft by moving a pump displacement control lever over center to the $-\gamma$ swash angle. This results in reversing the flow direction in the main power circuit as well as the direction of rotation of the motor shaft. Thus, the HST implements

continuously variable, proportional and reversible control of the HST output speed and transmitted power.

Referring to fig. 1, the charge pump 2 replenishes fluid losses due to oil leakages and compressibility through the make-up check valves 3. It maintains the low loop pressure by setting spring pretension in the charge pump relief valve 4, thereby ensuring the main pump is primed and does not cavitate. The cross relief valves 5 limit the maximum pressure level in the power circuit. The flushing shuttle valve 6 removes a certain volume of oil from the power contour through the flushing relief valve 7. The diverted oil flow must be made up by the charge pump. The oil diversion improves heat and contamination transfer out of the power contour. Often the charge pump and auxiliary valves are integrated within the main hydro-static pump Dan [2015c], Korn [1969].

In this study, only the power circuit of the HST was considered: since the main power transmitting elements of the HST are the pump and motor, the auxiliary valves and the charge pump were excluded from the study. Other assumptions are summarized as follows.

- The maximum displacements of the pump and the motor are equal, $V_{P.max} = V_{M.max}$;
- The pump displacement is infinitely variable in the range $[-V_{P.max}, V_{P.max}]$;
- The motor displacement is fixed $V_M = V_{M.max}$;
- Only the single-pump/single-motor configuration is considered, i.e. tandem or double arrangements either of a pump or a motor are out of scope of the study;
- The low loop pressure is maintained constant $p_l = \text{const}$;
- The effect of the connecting pipes and fittings is neglected.

2.2 HST efficiency

The power transmitting capacity of the HST is defined by displacements V of the machines it consists of: pump and motor with the corresponding displacements V_P and V_M respectively. The total efficiency of power transmission in the HST, its overall efficiency η_{HST} , depends on the efficiencies of each hydro-static machine: pump η_P and motor η_M efficiencies. In turn, the overall efficiency of the single displacement hydro-static machine is a product of volumetric η_v and mechanical η_m components. Lowercase subscripts “ v ” and “ m ” signify volumetric and mechanical efficiencies. The total pump and motor efficiencies are defined as follows:

$$\eta_P = \eta_{Pv}\eta_{Pm} \quad (1)$$

$$\eta_M = \eta_{Mv}\eta_{Mm} \quad (2)$$

The total HST efficiency η_{HST} can be presented in two ways: through the total efficiencies of the hydro-static machines it is made of or as a product of its volumetric and mechanical efficiencies:

$$\eta_{HST} = \eta_P \eta_M = \eta_{HSTv} \eta_{HSTm} \quad (3)$$

132 The actual pump discharge flow rate Q_{out} , the pressure difference across its ports Δp relate to
 133 the pump displacement V_P , the pump shaft speed n_P and torque T_P in a following manner.

$$Q_{out} = \eta_{Pv} n_P V_P \quad (4)$$

$$\Delta p = \frac{\eta_{Pm} T_P}{V_P} \quad (5)$$

134 Here $\Delta p = p_h - p_l$ is the pressure differential corresponding to the load-demanded pressure
 135 difference between the pump discharge and suction ports, which are the high- and low-pressure lines
 136 of the HST main power contour respectively.

137 Multiplication the left- and right-hand sides of eqs. (4) and (5) term by term results in the
 138 relation between the hydraulic power P_{hydr} of the oil leaving the pump and its input mechanical
 139 power P_{in} through the total pump efficiency η_P .

$$\underbrace{P_{hydr}}_{Q_{out} \Delta p} = \underbrace{\eta_P}_{\eta_{Pv} \eta_{Pm}} \underbrace{P_{in}}_{n_P T_P} \quad (6)$$

140 In the HST motor, the hydraulic power P_{hydr} is converted back into the output mechanical
 141 power of the rotating motor shaft P_{out} with some power loss defined by the total motor efficiency
 142 η_M .

$$\underbrace{P_{out}}_{n_M T_M} = \underbrace{\eta_M}_{\eta_{Mv} \eta_{Mm}} \underbrace{P_{hydr}}_{Q_{out} \Delta p} \quad (7)$$

143 Here n_M, T_M – motor shaft speed and torque respectively. Motor speed n_M and torque T_M
 144 related to the hydraulic power components $Q_{out}, \Delta p$ and the motor displacement V_M in a similar
 145 way as eqs. (4) and (5) do.

$$Q_{out} = \frac{n_M V_M}{\eta_{Mv}} \quad (8)$$

$$\Delta p = \frac{T_M}{\eta_{Mm} V_M} \quad (9)$$

146 Note, that eq. (7) can be obtained multiplying eqs. (8) and (9) as well.

147 From eqs. (6) and (7) the relation between the HST output mechanical power P_{out} to its input
 148 mechanical power P_{in} through the total HST efficiency η_{HST} can be defined as:

$$\underbrace{P_{out}}_{n_M T_M} = \underbrace{\eta_{HST}}_{\underbrace{\eta_{HSTv} \eta_{HSTm}}_{\eta_{Pv} \eta_{Mv} \eta_{Pm} \eta_{Mm}}} \underbrace{P_{in}}_{n_P T_P} \quad (10)$$

149 It follows from eq. (10) that in order to describe the power transmitting capability of the HST,
 150 both the volumetric and mechanical components of both the pump and motor efficiencies need to be
 151 quantified first.

152 3 Axial piston machine

153 3.1 APM operation

154 The most common class of positive displacement machines used in the HST is a swash plate axial
 155 piston machine (APM), in which the pistons are reciprocating parallel to the drive shaft axis.
 156 The APM design is widely used due its compactness, robustness as well as its ability to operate
 157 with higher efficiencies and high powers than other types of positive displacement machines. The
 158 schematic of a rotating group with pumping elements of a typical APM is illustrated in fig. 2.

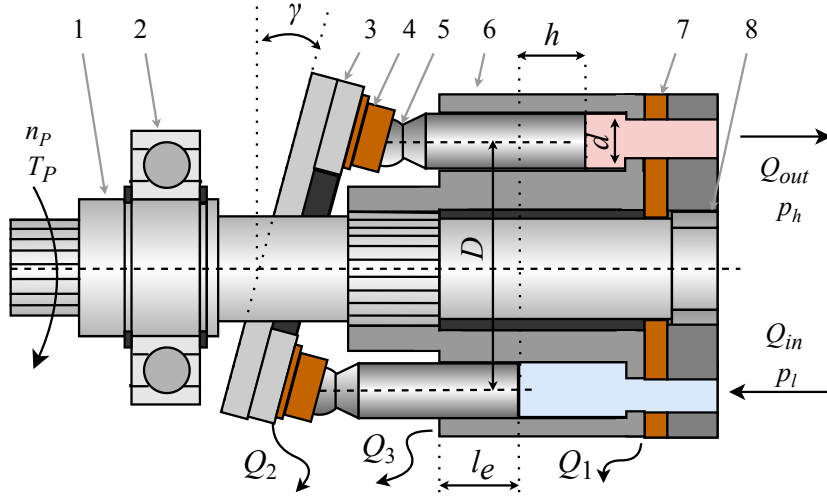


Figure 2: Rotating group of an APM

159 The pump receives power from a prime mover, which drives the pump shaft 1 through the end
 160 splines. The shaft is located in the pump housing, not shown on the diagram, and supported by

the bearings 2 and 8, which carry loads from the shaft and ensure its free rotation. The middle shaft splines transfer rotation to the cylinder block 6, which houses a set of pistons 5 equidistantly spaced along the pitch circle diameter, PCD. The pistons 5 are attached to slippers 4 with a ball joint. Each slipper slides along the swash wear plate 3 tilted by the swash angle γ . The hold-down force pushing slippers to the swash plate 3 is ensured either by a hydro-static pressure force, or by a hold-down ring (not shown). The rotating cylinder block 6 slides along the fixed valve plate 7. Tightness of this interface is achieved by the clamping force resulted from the high pressure in the piston chambers.

The drive shaft, the cylinder block and the piston-slipper assemblies have the same axis of rotation and the angular speed n_P around it. At every shaft revolution each piston performs single suction and discharge strokes. In fig. 2 the chambers are depicted in their extreme positions: the top and bottom dead centres, or TDC and BDC respectively.

According to fig. 2, the former corresponds to the smallest volume of the piston chamber. During the first half turn of the cylinder block, the chamber travels from the TDC towards BDC. As the slippers are clamped to and slide along the swash plate, the slippers pull the pistons out of the chamber. This results in chamber expansion, which causes the oil to be drawn into the chamber. Expanding chambers over time create the total pump suction flow rate Q_{in} . When the piston chamber reaches the BDC, the chamber volume increases to its maximum and the suction stroke is completed. During the second half turn, the chamber volume decreases, the oil is being displaced by the retracting pistons with the total flow rate Q_{out} . Therefore, during one shaft revolution the pump discharges the oil volume equal to the pump displacement V_P .

The displacement V is a geometric feature of any displacement machine, which is equal to the amount of displaced fluid per single revolution. For a piston machine, its displacement depends on the number of pistons z , the cross sectional area of the piston A_p and its stroke length h . For the APM, it takes the following form:

$$V = z \underbrace{\frac{\pi d^2}{4}}_{A_p} \underbrace{D \tan \gamma}_h \quad (11)$$

In this study, the following assumptions regarding the APM were made.

- Only the swash or slipper APM type design is considered further;
- The pistons and block bores are concentric;
- The oil leakage through the spherical piston/slipper interface is neglected;
- The slipper base and the swash plate are parallel, as well as the cylinders block plane surface and the valve plate;
- The slipper spin around its own axis is negligible Zhang et al. [2017];

- The shoulder width t on the block plane face is the same for the inner and outer port lands, i.e. $t = R_{bo} - r_{bo} = R_{bi} - r_{bi}$, see fig. 3;
- Contribution of a single piston chamber to flow rate and pressure fluctuations are neglected. The volume flow rate and the pressure difference in the main power circuit of the HST are considered directly proportional to the machine displacement and time-invariant.

3.2 Sizing

In order to quantify any performance characteristic of the APM and its efficiency η specifically, the key dimensions of the piston chamber, see fig. 3, need to be established beforehand. For that reason the basic sizing of the piston 3, the cylinder block 4, the slipper 2 and the valve plate 5 preceded efficiency calculations. The sizing followed the design procedure Manring [2013], which is based on the chosen APM displacement V , the swash angle γ , the number of pistons z and balance coefficients k_1, \dots, k_5 .

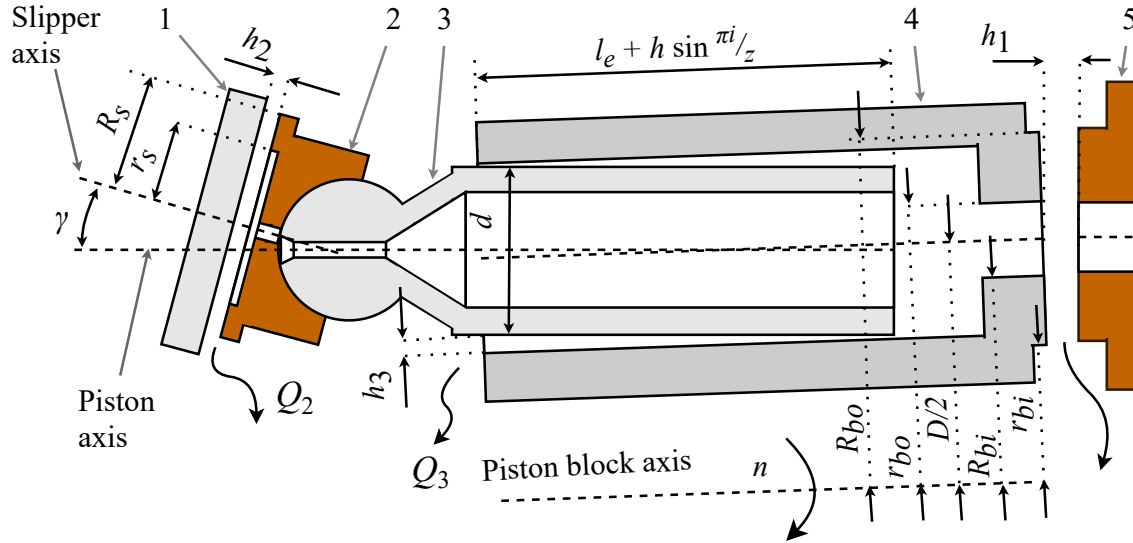


Figure 3: Piston chamber

The key sizes of the piston chamber defining the volumetric efficiency of the pump η_{P_v} include the piston diameter d , which corresponds nominally to the cylinder block bore diameter,

$$d = \sqrt[3]{\frac{4k_1 V_P}{z^2 \tan \gamma}} \quad (12)$$

the pitch circle diameter D of the bores on the cylinder block,

$$D = \frac{zd}{\pi k_1} \quad (13)$$

the kidney-shaped port width $w = r_{bo} - R_{bi}$,

$$w = \frac{2 \left(-d + \sqrt{d^2 + k_3 A_p (\pi - 4)} \right)}{\pi - 4} \quad (14)$$

the width t of the symmetrical sealing shoulder on the block and the valve plate,

$$t = \frac{k_2 z A_p}{\pi D} - w \quad (15)$$

and the slipper external R_s and internal r_s radii.

$$R_s = \frac{\pi D k_5}{2z} \quad (16)$$

$$r_s = \sqrt{R_s^2 - \frac{4k_4 A_p}{\pi \cos \gamma}} \quad (17)$$

The design features on fig. 3 and their sizes constitute the minimum necessary geometry required to initially estimate the overall power efficiency of the APM.

3.3 Volumetric efficiency

Generally the volumetric efficiency η_v is determined by the ratio of the actual discharge flow rate Q_{out} to the theoretical one Q_{th} .

$$\eta_v = \frac{Q_{out}}{Q_{th}} \quad (18)$$

The theoretical volume flow rate Q_{th} is the amount of non compressible oil displaced by the ideal machine, which operates with no volumetric fluid losses. For the pump it can be expressed as follows.

$$Q_{Pth} = n_P V_P \quad (19)$$

The actual pump discharge volume flow rate is defined through the theoretical volume flow rate Q_{Pth} , the amount of oil it losses due to leakages Q_L and the oil bulk modulus β Manring [2013], Rabie [2009]:

$$Q_{out} = \left(1 - \frac{\Delta p}{\beta} \right) Q_{Pth} - Q_L \quad (20)$$

222 The second term in the brackets in eq. (20) represents the oil volumetric losses due to its
 223 compressibility. The pump performs additional work to compress the oil as it goes from the low
 224 intake pressure p_l to the high discharge pressure p_h Manring [2013].

225 Combining eqs. (19) and (20) with eq. (18) determines the pump volumetric efficiency

$$\eta_{Pv} = 1 - \frac{\Delta p}{\beta} - \frac{Q_L}{Q_{Pth}} \quad (21)$$

226 In eqs. (20) and (21), the total leakage flow rate Q_L is the sum of leakage flow rates occurring
 227 through each gap between the pump wetted moving parts, which are adjacent to the pumping
 228 chamber. In this study three interfaces and associated leakage flow rates are considered: block-valve
 229 plate Q_1 , slippers-swash plate Q_2 and pistons-bores Q_3 , see figs. 2 and 3. The total leakage then
 230 becomes:

$$Q_L = \sum_{i=1}^3 Q_i \quad (22)$$

231 The leakage flow rates estimation has become a classical topic in pump performance studies. To a
 232 large extent this is due to the direct effect leakages have on the machine volumetric efficiency η_v . The
 233 academic research resulted in a variety of mathematical models differing in fidelity of mathematical
 234 representations and included physical phenomena Bergada et al. [2012], Xu et al. [2016]. The
 235 common is the assumption of a laminar flow in the thin interface gap, i.e. the Hagen-Poiseuille flux
 236 White [2011].

237 According to the Hagen-Poiseuille description of the laminar flow in narrow channels and referring
 238 to fig. 3, the leakage flow rate Q_1 between the block and the valve plate, leakage Q_2 through the
 239 slipper-swash plate interface and leakage Q_3 through the piston-bore clearances are defined as
 240 follows.

$$Q_1 = \frac{\pi h_1^3}{6\mu} \frac{p_h + p_l}{2} \left(\frac{1}{\ln \frac{R_{bo}}{r_{bo}}} + \frac{1}{\ln \frac{R_{bi}}{r_{bi}}} \right) \quad (23)$$

$$Q_2 = \frac{\pi z h_2^3}{6\mu} \frac{p_h + p_l}{2} \frac{1}{\ln \frac{R_s}{r_s}} \quad (24)$$

$$Q_3 = \frac{\pi d h_3^3}{12\mu} \left(1 + \frac{3}{2} \left(\frac{e}{h_3} \right)^3 \right) \frac{p_h + p_l}{2} \sum_{i=0}^{z-1} \frac{1}{l_e + h \sin \frac{\pi i}{z}} \quad (25)$$

241 Equations (23) and (24) define a planar radial Hagen-Poiseuille laminar outflow. The leakage
 242 flows Q_1 and Q_2 exist for each piston-slipper assembly. Therefore, eqs. (24) and (25) include the
 243 number of pistons z . Equation (25) describes the laminar flow in a non-concentric annular pipe with
 244 eccentricity e .

245 The oil properties are accounted for by the dynamic viscosity μ . In this research, the effect of
 246 temperature on viscosity and efficiency is not considered. Hence, both dynamic viscosity μ and the
 247 oil bulk modulus β are regarded as constant parameters, see table 1.

248 In eq. (23), radii r_{bi} , R_{bi} and r_{bo} , R_{bo} define the width of inner and outer sealing lands on the
 249 base plane of the cylinder block. These radii correspond to the length of the leakage channel in a
 250 planar radial outflow. Accordingly, r_s , R_s in eq. (24) signify the radius of the slipper pocket in its
 251 base and its outer radius respectively.

252 In eq. (25), the geometry of the annular leakage channel is specified by the piston-bore engagement
 253 length $l_e + h \sin(\pi i/z)$ and the piston radial clearance h_3 , which becomes a channel height for the
 254 unfolded annulus. Due to block rotation and piston reciprocating motion, the engagement length
 255 for each piston ranges from the minimum engagement length $l_e = 1.4d$, see figs. 2 and 3, to the
 256 maximum piston retraction into the bore $l_e + h$, where h is the piston stroke, see eq. (11). The
 257 thickness of the oil film in the annulus, or the channel height, is also influenced by the piston-bore
 258 axes offset, or their eccentricity $e \in [0, h_3]$. In this study, the axes of the bores and pistons are
 259 assumed eccentric, but parallel.

260 According to the set of assumptions for efficiency estimation, the oil film thicknesses h_1 , h_2
 261 and h_3 in each gap are constant along the length of a channel. According to eqs. (23) to (25),
 262 the size of the clearance is the most impactful factor in overall performance of the APM. Each
 263 interface performs two equally crucial functions in APM operation: sealing and lubrication. The
 264 former defines amount of leakage and thereby the volumetric efficiency η_v . The latter ensures the
 265 hydro-dynamic nature of friction between the moving parts forming the interface contributing to
 266 high mechanical efficiency η_m as well.

267 In calculation of the volumetric efficiency of the motor η_{Mv} , oil compressibility term does not
 268 contribute to volumetric losses as the oil is delivered to the motor already compressed. The other
 269 factors in leakage estimation followed the same logic as for the pump.

$$\eta_{Mv} = 1 - \frac{Q_L}{Q_{Mth}} \quad (26)$$

270 3.4 Mechanical efficiency

271 In this research a semi-empirical model of the mechanical efficiency η_m was used as the full tribological
 272 losses in the APM are notoriously hard to predict Hasko et al. [2019]. Evaluation and analysis of
 273 these losses is the subject of active ongoing researches Li et al. [2017], Chen et al. [2019].

274 The employed model originates from the Stribeck curve, which is the common descriptor of the
 275 friction coefficient behavior in mechanical interfaces with mixed lubrication between the moving
 276 parts. The model considers three possible lubrication modes: boundary, mixed and hydrodynamic.

Parameter	Symbol	Pump	Motor	Units
PCD balance	k_1	0.75	0.75	
Cylinder block balance	k_2	0.9	0.9	
Kidney area balance	k_3	0.45	0.45	
Slipper balance	k_4	0.93	0.93	
PCD-slipper balance	k_5	0.75	0.75	
Efficiency coefficient	A	0.17	0.17	
Efficiency coefficient	B	1	0.5	bar deg/cP rpm
Efficiency coefficient	C	0.001	0.005	$\sqrt{\text{bar deg/cP rpm}}$
Efficiency coefficient	D	125	125	bar deg
Number of pistons	z	9	9	
Swash angle	γ	18	18	deg
Valve plate clearance	h_1	29	29	μm
Slipper clearance	h_2	29	29	μm
Radial piston clearance	h_3	25	25	μm
Piston axes offset	e	25	25	μm
Low side pressure	p_l	25		bar
Oil bulk modulus	β	1.1		GPa
Dynamic viscosity	μ	12.86		mPa s

Table 1: Design balances and coefficients in the efficiency model

It simulates the exponential decay of the friction coefficient in the boundary and mixed regions, followed by its square-root rise proportional to the Hersey number Manring [2013]. The assumption results in the following expression of the approximate pump mechanical efficiency.

$$\eta_{Pm} = 1 - A_P \exp\left(-\frac{\mu n_P B_P}{\Delta p \gamma}\right) - C_P \sqrt{\frac{\mu n_P}{\Delta p \gamma}} - \frac{D_P}{\Delta p \gamma} \quad (27)$$

Here A_P , B_P , C_P and D_P are empirical, experimentally determined coefficients. The suggested values Manring [2013] are listed in table 1. The motor mechanical efficiency differs from the pump one in eq. (27) by the model coefficients and the motor speed n_M . Due to volumetric losses in both APMs in the HST, the motor output speed is inevitably smaller than the pump one. The extent of this inequality is defined by the total volumetric efficiency of the HST η_{HSTv} and the ratio of pump and motor displacements V_P and V_M respectively, see eqs. (4) and (8). The motor shaft speed and the motor mechanical efficiency are defined as follows.

$$n_M = \eta_{HSTv} n_P \frac{V_P}{V_M} \quad (28)$$

$$\eta_{Mm} = 1 - A_M \exp\left(-\frac{\mu n_M B_M}{\Delta p \gamma}\right) - C_M \sqrt{\frac{\mu n_M}{\Delta p \gamma}} - \frac{D_M}{\Delta p \gamma} \quad (29)$$

287 The set of eqs. (21), (26), (27) and (29) can be inserted into eq. (3) to complete the mathematical
 288 model of the overall HST efficiency η_{HST} . The necessary parameters for the efficiency calculation
 289 are summarized in table 1.

290 4 HST volumetric efficiency model validation

291 To validate the mathematical model of the HST efficiency, the sample of 778 measurements of the
 292 output shafts speeds of 196 cc/rev HSTs was analysed. The tested HSTs were driven at a constant
 293 pump speed of 1780 rpm, primed with SAE 30 oil at 60°C with 14 bar of charge pressure. The
 294 motor shaft load was developing 207 bar of the discharge pressure in the high-pressure line of the
 295 tested HSTs. With the measured motor speed and known pump speed, the volumetric efficiency was
 296 calculated as the shafts speed ratio.

297 The actual measurements were performed on 389 HSTs, with two measurements per transmission.
 298 One corresponded to the forward mode, at which the pump and motor shafts rotated in the same
 299 direction. The second measured the motor speed at opposite shafts rotation, or backward, mode.
 300 The former mode characterized by the positive pump swash angle resulted in the swash plates of the
 301 pump and motor being parallel to each other. The latter mode was ensured by inclining the pump
 302 swash plate to the negative angles, in which case the pump and motor swash plates were not aligned.

303 The test HST geometry needed as the input to the efficiency model was directly measured
 304 from the actual parts. Using the measured design balances reconstructed from the dimensions
 305 measurements and the known test conditions, the calculation of the volumetric efficiency was
 306 performed for the maximum and minimum piston-bore clearances according to the mathematical
 307 model in sections 2.2, 3.3 and 3.4. The maximum and minimum piston-bore clearance resulted from
 308 the manufacturing tolerances applied to the piston outer diameter and cylinder block bores. The
 309 parameters of the tested HST and test conditions specification used in validation are summarized in
 310 table 2.

311 The nominal size of the piston-bore gap can be obtained from the manufacturing drawings of the
 312 parts. The outer piston diameter and the bore diameter are sized with appropriate manufacturing
 313 tolerances. Similar nominal dimensions and tolerances are notoriously hard to obtain for the slipper-
 314 swash plate and block-valve plate interfaces. The actual oil thicknesses, the interface gaps are less
 315 predictable comparing with the piston-bore. Moreover, the slipper-swash and block-valve plate

Parameter	Value	Units
Sample size	778	
Test HST displacement	196	cc/rev
Swash angle	15	deg
Number of pistons	9	
Min radial piston-bore clearance	23	μm
Max radial piston-bore clearance	34	μm
Pump speed	1780	rpm
Charge pressure	14	bar
Discharge pressure	207	bar
Oil	SAE30	
Oil temperature	60	$^{\circ}\text{C}$
Oil dynamic viscosity	30.58	mPa s

Table 2: Parameters of the test HSTs and test conditions

clearances depends to a higher extent on operating conditions of a machine, than on manufacturing quality. As a result, the piston-bore clearance is the leakage pathway that, firstly, can be quantified with higher level of certainty; secondly, has strong effect on the efficiency, more than other controllable parameters. Therefore, the piston-bore clearance was used as the main parameter in the volumetric efficiency model to quantify the range of efficiencies the model predicts for the test HST design.

The distribution of the collected test data recalculated to the HST volumetric efficiency is plotted in fig. 4 with Hunter [2007], Waskom [2021] as the measurements count histogram with corresponding kernel density estimation (KDE) function. Figure 4 illustrates the test data mean $\mu = 88.52\%$ with the standard deviation $\sigma = 0.63\%$ and $\mu \pm \sigma$ range.

The two outermost dashed lines on fig. 4 correspond to the extreme values of the piston-bore clearance. The volumetric efficiency of the HST with the aforementioned geometrical assumptions and operating at the specified test conditions is calculated to fall in a range from 84.83% to 93.61% limited by the maximum and minimum values of the piston-bore clearance. The test mean is 0.37% away from the model predicted average volumetric efficiency. The predicted volumetric efficiency range encloses the entire test data with reasonable margins. This validates model fidelity, accuracy and the overall capability to predict the HST volumetric efficiency.

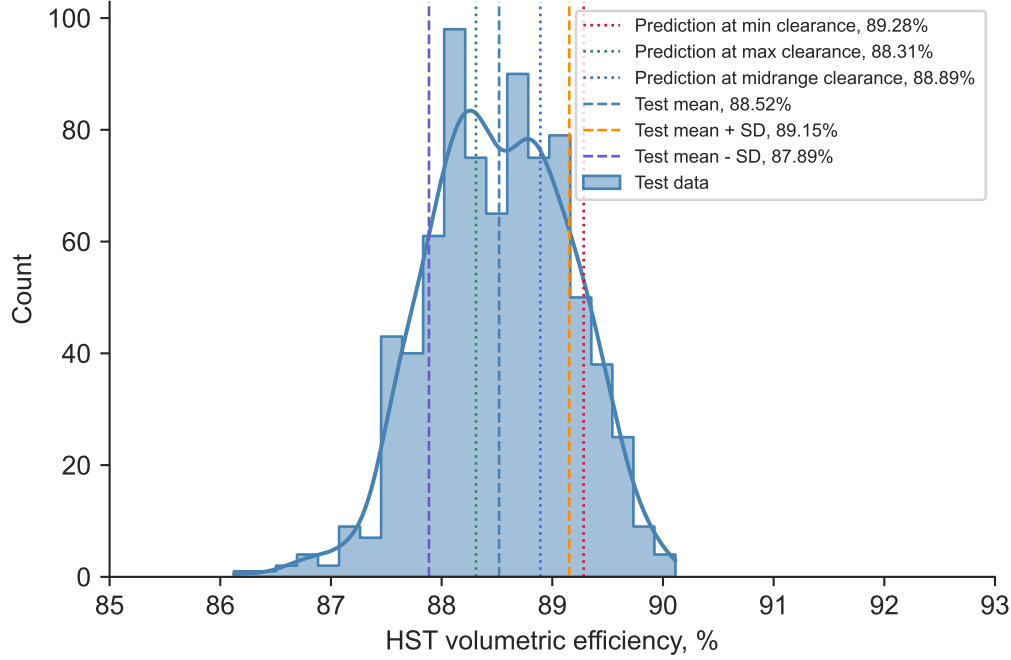


Figure 4: HST volumetric efficiency model validation. Test data: $N = 778$, $\mu = 88.52\%$, $\sigma = 0.63\%$

5 Optimization

The main goal of the product definition stage during the HST development is specification of the key design parameters of the APMs Dan [2015a]: its overall size, which is driven by its maximum displacement V , rated shaft angular speed n and rated pressure differential Δp . A combination of these will define the following stages of the design development process. For example, the structural strength and integrity analysis will primarily be driven by the loads generated for the selected sizes and the maximum pressure differential.

At the same time, the most common vehicle requirements to the HST are its efficiency η_{HST} , the output power P_{out} and its overall mass m_{HST} . The goal on the preliminary design specification stage is to maximize efficiency and transmitted power, minimizing the overall weight subject to speed performance constraint. In other words, it is desirable to ensure the highest possible power density within the smallest possible package subject to the engine speed limitations.

344 5.1 Problem formulation

345 The posed problem above represents an example of a multi-objective (MO), multi-variable constrained
 346 optimization problem, which in general terms can be states as follows Deb [2011].

$$\begin{aligned}
 & \text{minimize } f_m(\mathbf{x}), \quad m = 1, \dots, M; \\
 & \text{subject to } g_j(\mathbf{x}) \leq 0, \quad j = 1, \dots, J; \\
 & \quad \quad \quad h_k(\mathbf{x}) = 0, \quad k = 1, \dots, K; \\
 & \quad \quad \quad x_i^{(L)} \leq x_i \leq x_i^{(U)}, \quad i = 1, \dots, I.
 \end{aligned} \tag{30}$$

347 A solution $\mathbf{x} = (x_1, \dots, x_I)^T \in \mathbb{R}^I$ to the MO problem is a decision vector of I decision variables.
 348 Those solutions satisfying the variable upper $x_i^{(U)}$ and lower $x_i^{(L)}$ bounds constitute a decision
 349 variable search space $\mathcal{S} \subseteq \mathbb{R}^I$.

$$\mathcal{S} = \left\{ \mathbf{x} : x_i^{(L)} \leq x_i \leq x_i^{(U)}, \forall i \in \mathbb{N}_{\geq 0}^{\leq I} \right\} \tag{31}$$

350 The solutions from the search space \mathcal{S} , which satisfy further to J inequality constraints $g_j(\mathbf{x})$
 351 and K equality constraints $h_k(\mathbf{x})$ define a feasible search space $\mathcal{F} \subseteq \mathcal{S}$.

$$\mathcal{F} = \left\{ \mathbf{x} : g_j(\mathbf{x}) \leq 0 \wedge h_k(\mathbf{x}) = 0, \forall \mathbf{x} \in \mathcal{S}, \forall j \in \mathbb{N}_{\geq 0}^{\leq J}, \forall k \in \mathbb{N}_{\geq 0}^{\leq K} \right\} \tag{32}$$

352 A single objective function is defined as $f_m(\mathbf{x}) : \mathbb{R}^I \rightarrow \mathbb{R}$. The vector objective function $\mathbf{f}(\mathbf{x})$
 353 produces an image of the decision vector \mathbf{x} from the search space \mathcal{S} to objective space \mathcal{O} .

$$\mathbf{f} : \mathbf{x} \in \mathcal{F} \rightarrow \mathbf{y} \in \mathcal{O} \tag{33}$$

354 The resultant objective vector $\mathbf{y} = \mathbf{f}(\mathbf{x}) = (f_1(\mathbf{x}), \dots, f_m(\mathbf{x}))^T \in \mathcal{O} \subseteq \mathbb{R}^M$ constitutes the M -
 355 dimensional objective space $\mathcal{O} \subseteq \mathbb{R}^M$:

$$\mathcal{O} = \{ \mathbf{y} : \mathbf{y} = \mathbf{f}(\mathbf{x}), \forall \mathbf{x} \in \mathcal{F} \} \tag{34}$$

356 To solve the MO optimization problem means to identify such a set \mathbf{X}_p of the decision vectors \mathbf{x}_p
 357 from the feasible solutions set \mathcal{F} , that the corresponding set \mathbf{Y}_p of the objective vectors or images \mathbf{y}_p
 358 from the objectives space \mathcal{O} forms the non-dominated or Pareto front. Domination of one objective
 359 vector \mathbf{y}_p over another \mathbf{y} for the minimization problem is defined as

$$\mathbf{y}_p \prec \mathbf{y} \iff \left(f_m(\mathbf{x}_p) \leq f_m(\mathbf{x}), \forall m \in \mathbb{N}_{\geq 0}^{\leq M} \right) \wedge \left(\exists m \in \mathbb{N}_{\geq 0}^{\leq M} : f_m(\mathbf{x}_p) < f_m(\mathbf{x}) \right) \tag{35}$$

360 The sets \mathbf{X}_p and \mathbf{Y}_p are referred to as the Pareto-optimal set and front respectively. These can
 361 be defined as the following Engelbrecht [2007]

$$\mathbf{X}_p = \{\mathbf{x}_p \in \mathcal{F} : \forall \mathbf{x} \in \mathcal{F}, \mathbf{f}(\mathbf{x}_p) \prec \mathbf{f}(\mathbf{x})\} \quad (36)$$

$$\mathbf{Y}_p = \{\mathbf{y}_p \in \mathcal{O} : \mathbf{y}_p = \mathbf{f}(\mathbf{x}_p)\} \quad (37)$$

362 In other words, the problem consists in identifying such bounded allocations of the pump
 363 maximum displacement V_P , its shaft rated angular speed n_P and its pressure differential Δp that
 364 the corresponding total HST efficiency η_{HST} , output power P_{out} and its total mass m_{HST} result
 365 in the Pareto efficient combination given that the pump speed n_P does not exceed the speed limit
 366 $n_{P,lim}$.

367 5.2 Decision variables

368 According to the preceding considerations, the decision vector \mathbf{x} for the problem above

$$\mathbf{x} = (V_P, n_P, \Delta p)^T \in \mathbb{R}^I, i \in \mathbb{N}_{\geq 0}^{\leq I} \quad (38)$$

369 A set of variables bounds $x_i^{(L)}, x_i^{(U)}$ contracts the solutions space \mathbb{R}^I to the search space $\mathcal{S} \subseteq \mathbb{R}^I$.
 370 The bounds are represented by the lower and upper boundary vectors:

$$\mathbf{x}^{(L)} = (V_{P,min}, n_{P,min}, \Delta p_{min})^T \quad (39)$$

$$\mathbf{x}^{(U)} = (V_{P,max}, n_{P,max}, \Delta p_{max})^T \quad (40)$$

371 5.3 Pump speed constraint

372 The displacement V of the APM limits its operational speed n due to the risk of cylinder block
 373 lifting caused by axially unbalanced centrifugal forces from the rotating piston-slipper assemblies.
 374 Exceeding the maximum speed at high swash angles results in separation of the block from the valve
 375 plate on one side and metal-to-metal frictional contact on the other side of the block. This eventually
 376 can lead to loss of drive power Manring [2013], to dangerously high and uncontrollable motor shaft
 377 angular speeds. Exceeding allowable shaft angular speeds also results in heightened linear reciprocal
 378 piston speeds and cavitation. The high-speed cavitation problem continues to draw attention of
 379 the research community as it renders a relatively straightforward way to improve power density of
 380 hydraulics Wang [2010], Chao et al. [2019], Vacca et al. [2010]. For the reasons above, operation
 381 above the maximum speed limit must be avoided under all modes of operation Dan [2015b].

382 The speed limitation imposes the nonlinear inequality performance constraint $g(\mathbf{x}) \leq 0$ since the
 383 feasible range of pump speeds n_P must be limited by the maximum allowable speed $n_{P.lim}$, which
 384 depends on the pump displacement V_P .

$$n_P \leq n_{P.lim}(V_P) \quad (41)$$

385 5.4 Catalogues data

386 In order to express the pump speed limit $n_{P.lim}$ explicitly as the inequality of the design vector
 387 components x_i , the data was collected from manufacturers catalogues relating the APM displacement
 388 and its rated speed, see fig. 5. The catalogue rated speed was considered as the maximum allowable
 389 pump $n_{P.lim}$ and motor $n_{M.lim}$ speeds. Each data point consisted of a triple of the machine
 390 displacement, rated speed, and weight. It can be noted, that majority of the collected data points
 391 correspond to small and medium sized APMs with displacements up to 150-200 cc/rev.

392 The middle dashed line in figs. 5a and 5b correspond to the exponential decaying regression model,
 393 which was fitted to the collected scattered data according to the non-linear least squares method
 394 Virtanen et al. [2020]. Figures 5a and 5b include individual KDE functions for each manufacturer
 395 along the axes built with the seaborn library Waskom [2021]. The KDEs visualize the spread and
 396 variance of each manufacturer's data along the variable axis.

397 Utilization of the catalogue data and regression models to predict the pump speed limit as well
 398 as the pump and motor mass based just on the machine displacement was proposed before Wu
 399 et al. [2017]. Although in the current study a combination of linear and exponential functions was
 400 proposed to describe the underlying data pattern, rather than a power function.

$$n_{P.lim}(V_P) = a_1 \exp(-a_2 V_P) + a_3 \quad (42)$$

401 Thus, the nonlinear inequality constraint takes the following exponential form from eqs. (41)
 402 and (42).

$$n_P - a_1 \exp(-a_2 V_P) - a_3 \leq 0 \quad (43)$$

403 Here a_1 , a_2 and a_3 are the coefficients of the fitted inequality constraint regression function $g(\mathbf{x})$.

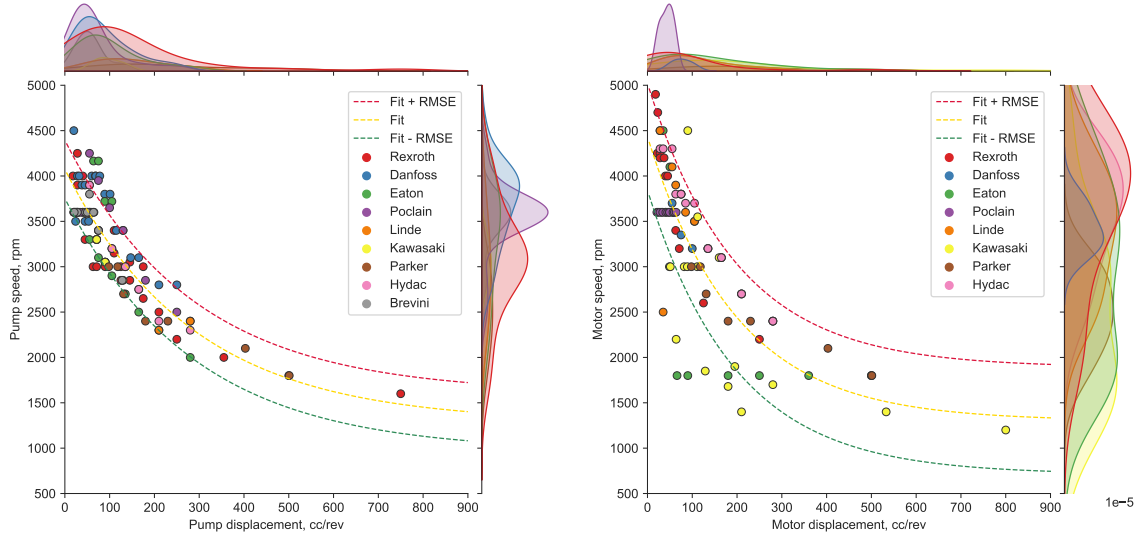
404 The coefficients are summarized in table 3.

405 The applied five-fold cross-validation Pedregosa et al. [2011], Devore [2011] resulted in the test
 406 root mean square error (RMSE) of the regression models equal to $RMSE_{np} = 320.59$ rpm for the
 407 pump maximum allowable speed model and $RMSE_{nm} = 589.01$ rpm for the motor speed model.
 408 In fig. 5c the count histograms and the KDE functions for the original pump and motor data are

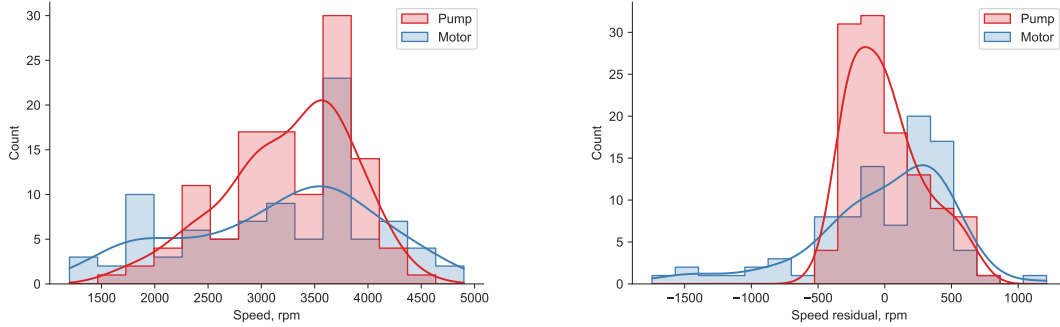
409 plotted, where higher variance of the motor data can be noted. The RMSE was estimated according
 410 to the following equation.

$$\text{RMSE} = \sqrt{\frac{1}{N} \sum_{i=1}^N (y_i - \hat{y}_i)^2} \quad (44)$$

411 Here N – the sample size ($N_p = 116$ variable pumps and $N_m = 91$ fixed motors for closed circuit



(a) Regression model of the original pump speed data: $N_p = 116$, $\text{RMSE}_{np} = 320.59$ rpm, $R_{np}^2 = 0.789$ (b) Regression model of the original motor speed data: $N_m = 91$, $\text{RMSE}_{nm} = 589.01$ rpm, $R_{nm}^2 = 0.552$



(c) Histograms of the original data for speed models (d) Histograms of the residuals of speed models

Figure 5: Empirical regression models and errors of the fits of the speed constraint models

systems), y_i – the individual target value of the i -th data point, \hat{y}_i – the modelled or predicted value for the i -th data point, $y_i - \hat{y}_i$ – the model residuals.

Figures 5a and 5b include the dashed lines above and below the fitted regression model, which indicate a tolerance zone one test RMSE away from the mean predicted value. Figure 5c illustrates how the original speed data is distributed for the pumps and motors. It indicates that the collected pump and motor speed data both peak at around 3500 rpm. That highlights prevalence of low displacement, high speed APMs in the sample.

The histograms in fig. 5d illustrate how the model residuals are distributed around zero, which corresponds to the model prediction. The pump data is skewed slightly to the negative regions, which means the regression model overestimates the data. The opposite applies to the motor data, it is skewed to the positive residuals although with wider variance than the pump data. Residuals skewness can be attributed to a tendency of manufacturers to assign a single value of a maximum rated speed as well as a mass to a range of displacements. Taking that into account, the overall quality of the regression models can be deemed as acceptable.

Much of observed variation in the original pump and motor data can be explained by the constructed regression models as indicated by the computed coefficients of determination estimated according to the expression below, see the R^2 values in the captions to figs. 5a and 5b.

$$R^2 = 1 - \frac{\sum_{i=1}^N (y_i - \hat{y}_i)^2}{\sum_{i=1}^N (y_i - \bar{y})^2} \quad (45)$$

The obtained values of data variance around the fitted curve and the coefficients of determination suggest appropriate accuracy of fitting. Therefore, the reasonable approximation of the data by the exponential function has been achieved.

5.5 Objectives

5.5.1 Total HST efficiency and transmitted power

The total efficiency η_{HST} , transmitted power P_{out} and weight m_{HST} requirements are common metrics of the HST performance. Therefore, these were selected as components of the vector-valued objective function $\mathbf{f}(\mathbf{x})$.

$$\mathbf{y} = \mathbf{f}(\mathbf{x}) = (-\eta_{HST}(\mathbf{x}), -P_{out}(\mathbf{x}), m_{HST}(\mathbf{x}))^T, \forall \mathbf{x} \in \mathcal{F} \quad (46)$$

The design goals are to improve the power density, i.e. to maximize the efficiency and power. Therefore, the negative sign of the efficiency $f_1 = -\eta_{HST}(\mathbf{x})$ and output power $f_2 = -P_{out}(\mathbf{x})$ objective functions is used for these objectives.

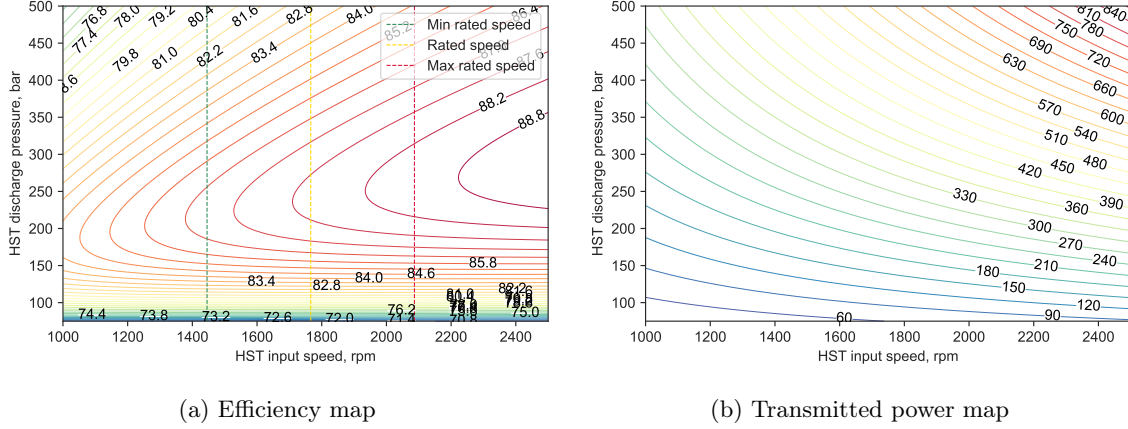


Figure 6: Efficiency and output power maps for an HST with $V_P = 500 \text{ cc/rev}$

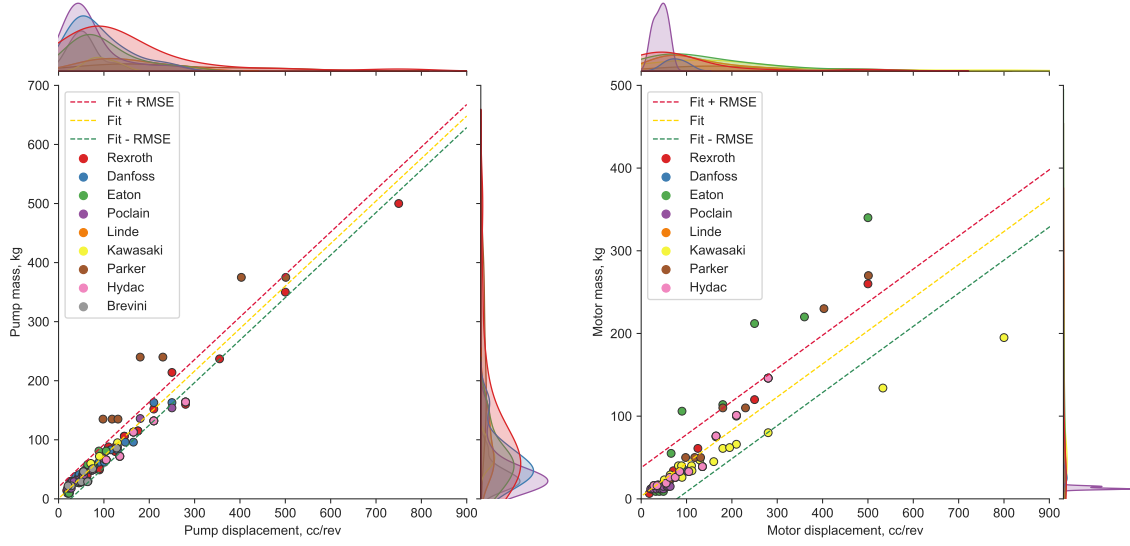
440 The decision vector \mathbf{x} in eq. (38), the set of assumed parameters in table 1 constitute the necessary
 441 information to calculate the basic sizes of the APM first according to eqs. (12) to (17), and then to
 442 compute the first two objective functions f_1 and f_2 according to eqs. (10), (21) to (27) and (29).

443 To demonstrate typical distributions of the HST efficiency and transmitted power, the overall
 444 HST efficiency η_{HST} and its output power P_{out} were calculated for the arbitrarily picked pump
 445 displacement $V_P = 500 \text{ cc/rev}$, although all the selected objective functions are positively correlated
 446 with the pump displacement V_P Xu et al. [2016], Vardhan and Dasgupta [2018], Liu et al. [2019].
 447 The resultant efficiency and power maps are depicted in fig. 6 as contour plots. The overall contour
 448 shapes follow expected behaviour of efficiency and power maps of a typical HST Manring [2016],
 449 which signifies satisfactory fidelity of the mathematical model.

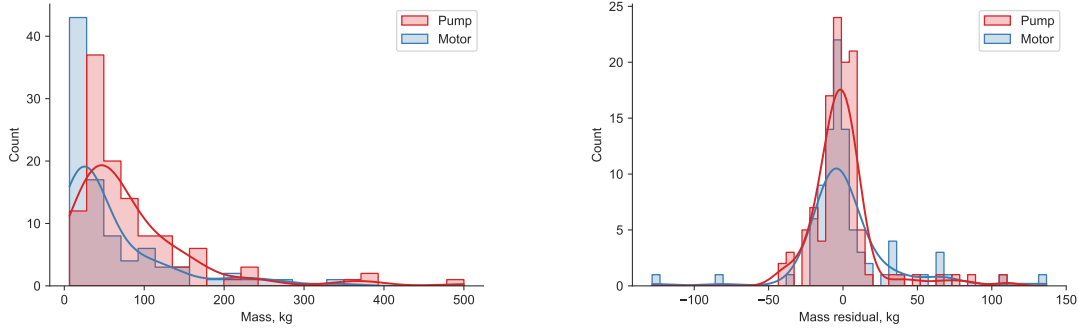
450 The pump speed regression model, its $\pm \text{RMSE}$ range for $V_P = 500 \text{ cc/rev}$ from fig. 5a are
 451 overlapped with the efficiency map in fig. 6a as the vertical dashed lines. These three lines are
 452 regarded as minimum, nominal and maximum rated pump speeds. The middle rated speed illustrates
 453 the boundary of the feasible space created by the pump speed constraint.

454 5.5.2 Total HST mass

455 The HST weight objective m_{HST} is linearly proportional to the displacement V_P and is not strictly
 456 affected by the other two variables at least on the preliminary design stage. In order to obtain the
 457 mass objective function formally, the manufacturers catalogue data was used, see figs. 7a and 7b.
 458 The ordinary linear least square method was be applied to approximate the empirical data for
 459 variable displacement pumps and fixed displacement motors to obtain linear dependencies $m_P(V_P)$
 460 and $m_M(V_M)$ Virtanen et al. [2020].



(a) Regression model of the original pump mass data, $N_p = 116$, $\text{RMSE}_{mp} = 19.48$ kg, $R_{mp}^2 = 0.933$ (b) Regression model of the original motor mass data, $N_m = 91$, $\text{RMSE}_{mm} = 34.64$ kg, $R_{mm}^2 = 0.830$



(c) Histograms of the original mass data (d) Histograms of the residuals of mass models

Figure 7: Empirical regression models and errors of fits of the mass objective models

$$m_P(V_P) = b_1 V_P + b_3 \quad (47)$$

$$m_M(V_M) = b_2 V_M + b_4 \quad (48)$$

Here b_1, \dots, b_4 are coefficients in the fitted regression models. Note, the mass of a variable displacement pump usually comprises masses of the main pump, a controller mechanism to adjust the swash plate angle and an integrated boost or charge pump with a relief valve. The data was

collected only for closed circuit mobile applications of APMs.

Due to the assumption of equality of the pump and motor displacements made in section 2, i.e. $V_{P,max} = V_{M,max}$, and neglecting effects of the auxiliary valves, the overall mass of the HST m_{HST} can be expressed as a function of just a single variable – the pump displacement V_P . Hence, summing eqs. (47) and (48) yields

$$m_{HST}(V_P) = (b_1 + b_2) V_P + b_3 + b_4 \quad (49)$$

To evaluate the regression models errors, the five-fold cross-validated test RMSEs were calculated for the pump and motor mass models according to the eq. (44) Pedregosa et al. [2011]. The resultant values of $RMSE_{mp} = 21.283$ kg and $RMSE_{mm} = 55.015$ kg for the pump and the motor respectively suggest reasonable accuracy of fitting. Variability of the motor mass relative to its displacement is almost two fold larger, than for the pump mass. Coefficient of determination indicate the appropriate quality of the linear regression models, see figs. 7a and 7b.

Figures 7c and 7d illustrate the spread of the original pump and motor mass data, and the regression models residuals respectively. As it was noted in the pumps and motor speed data, the collected original data gravitates towards smaller, up to 150 cc/rev, displacements, partly because the APMs with bigger displacements are more rare on the market. It can also be noted that the residuals are spread uniformly around the zero line, what suggest appropriate modelling capabilities of the built regression model.

The computed values of coefficients determination in table 3 suggest a strong linear dependency between the machine displacement and its mass and speed. The models are deemed as sufficiently accurate for the purpose of designing high displacement HST and relatively light to manipulate and calculate.

However, quality of the suggested regression models depicted in figs. 5a, 5b, 7a and 7b could have been improved further with acquiring and analyzing more data points, i.e. manufacturers' data for large displacement pumps and motors. This proved to be challenging as only few manufacturers venture to design and market machines with displacements above 300 cc/rev. That creates a lack of data points to be build more accurate and reliable regression models.

Moreover, some manufacturers group together machines in ranges of displacements and then assign a single value of a rated speed or a mass for the range. That creates horizontal lines on plots like figs. 5a, 5b, 7a and 7b, which do not reflect a physical nature of a speed limit or a mass-to-displacement dependency. Traces of these lines are also noticeable on errors plots figs. 5c and 7c, especially for the speed constraint figs. 5c and 5d.

From these plots a product focus of each manufacturer could be deduced. The common trend is prevalence of variable pumps over fixed motors in a product range breakdown, which is reflected

Parameter	Symbol	Value	Units
Coefficient in $n_P(V_P)$	a_1	2.7903×10^3	rpm
Coefficient in $n_P(V_P)$	a_2	3.5099×10^{-3}	rev/cc
Coefficient in $n_P(V_P)$	a_3	1.2835×10^3	rpm
Coefficient in $m_{HST}(V_P)$	b_1	0.70068	kg rev/cc
Coefficient in $m_{HST}(V_P)$	b_2	0.43174	kg rev/cc
Coefficient in $m_{HST}(V_P)$	b_3	1.9276	kg
Coefficient in $m_{HST}(V_P)$	b_4	1.2163	kg
Pump sample size	N_p	116	
Motor sample size	N_m	91	
RMSE of the pump mass model	$RMSE_{mp}$	19.48	kg
Coefficient of determination	R_{mp}^2	0.933	
RMSE of the motor mass model	$RMSE_{mm}$	34.64	kg
Coefficient of determination	R_{mm}^2	0.830	
RMSE of the pump speed model	$RMSE_{np}$	320.59	rpm
Coefficient of determination	R_{np}^2	0.789	
RMSE of the motor speed model	$RMSE_{nm}$	589.01	rpm
Coefficient of determination	R_{nm}^2	0.552	

Table 3: Parameters and quality of the regression models

in samples sizes in table 3. The collected data also shows that, an overall scatter of masses and speeds is larger for motors than pumps across all analyzed manufacturers. That indicates greater variability in design of fixed displacement motors, than in variable displacement pumps. Nonetheless, the analysis has demonstrated the APM displacement is a good predictor of its maximum rated speed as well as its mass. The regression models are able to account for a considerable portion of variability of speed and mass data, see coefficients of determination in table 3.

Figure 8 summarizes the calculation flow followed during optimization. The used parameters in the built mathematical models are listed in table 1, the coefficients and accuracy metrics of the regression models are in table 3.

5.6 Method

In this research, NSGA-II Deb et al. [2002] was used with the pymoo v.0.4.2 implementation Blank and Deb [2020]. The tournament selection and the self-adaptive simulated binary crossover Deb et al. [2007] with the distribution index $\eta_c = 15$ and the crossover probability $p_c = 0.2$ were used. The

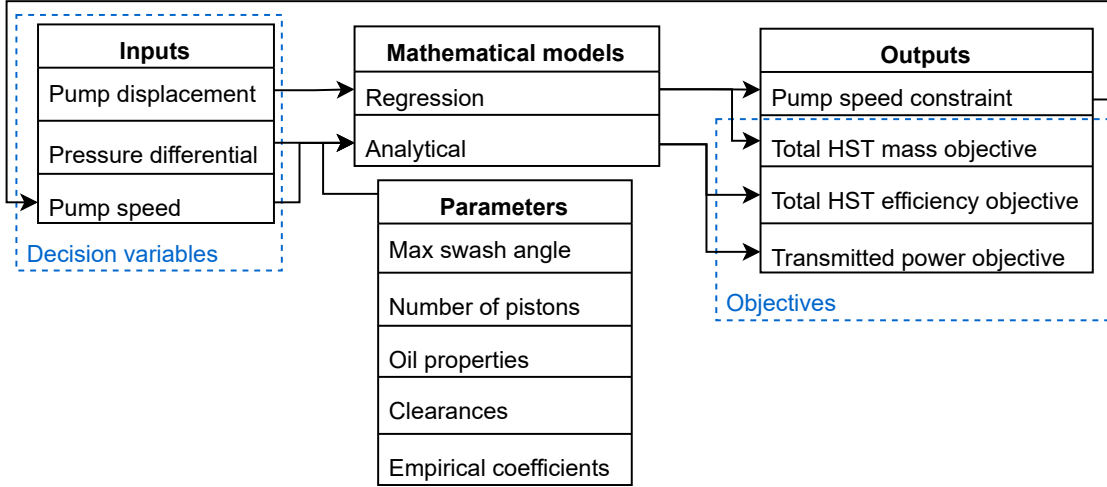


Figure 8: Calculations flowchart in optimization

high-tradeoff solutions were obtained with the pymoo decision making module realized according to the methodology proposed in Rachmawati and Srinivasan [2009] with some modifications Blank and Deb [2020], where the original tradeoff solutions search embedded in the optimization algorithm was replaced with post-processing function, rather the guiding one.

Parameter	Symbol	Value
Population size	N	400
Number of generations	n_{gen}	25
Number of objectives	M	3
Number of inequality constraints	J	1
Number of equality constraints	K	0
Number of decision variables	I	3
Upper bound of the decision vector	$\mathbf{x}^{(U)}$	(800, 3000, 700)
Lower bound of the decision vector	$\mathbf{x}^{(L)}$	(200, 1000, 100)

Table 4: NSGA-II parameters

The search space is limited by the lower and upper bounds of the decision vector, i.e. its components are within the following limits: pump displacement $V_p \in [200, 800]$ cc/rev, its speed $n_p \in [1000, 3000]$ rpm and pressure difference across its ports $\Delta p \in [100, 700]$ bar. The rest of the parameters used to set the NSGA-II are listed in table 4.

6 Results

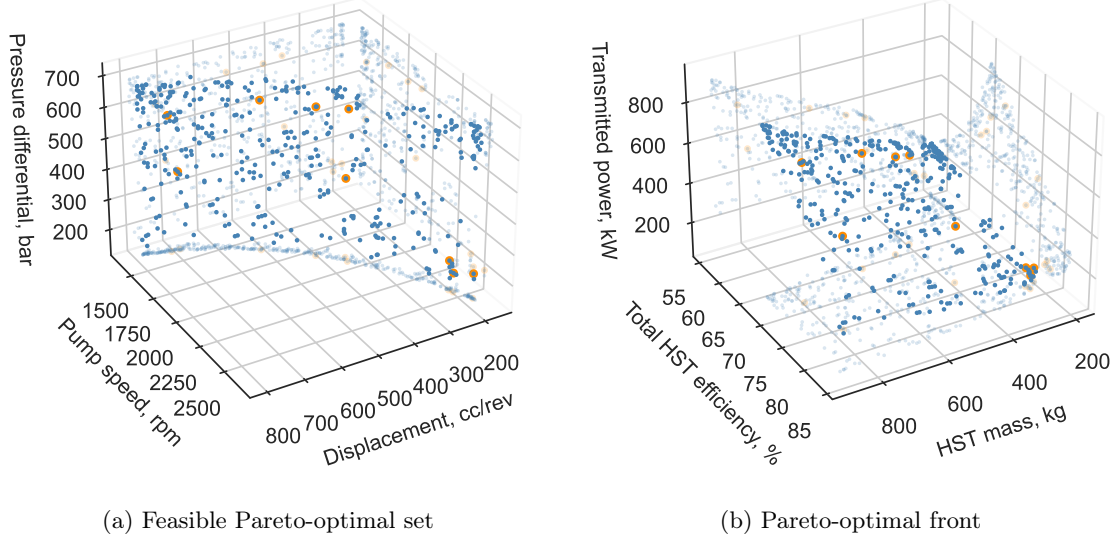


Figure 9: Optimization results

The solution of the optimization problem is the Pareto-optimal set of the design variables and the Pareto-optimal objectives front. Figure 9a illustrates the final state of the feasible Pareto-optimal set, after the generations count has reached the limit. It has been noted, that the Pareto-optimal solutions gravitate towards the cylindrical solutions surface, curvature of which defined by the exponential speed constraint. The high tradeoff solutions of the Pareto-optimal sets and fronts are highlighted in figs. 9 to 11.

The Pareto-optimal solutions tend to group along the decision variables boundaries, constraints and corners formed by these. It is the most noticeable on the pump speed-displacement projection of the Pareto set in fig. 10, where the non-dominated solutions follow closely the exponential speed limit constraint. It has also been noted, that the region along the high-pressure boundary is being populated densely with the solution, including high tradeoffs solutions.

The central regions of the final Pareto solutions distribution further from the extremes do not exhibit any pronounced concentration areas and remain relatively uniformly populated. Non-dominated solutions are fairly homogeneously spread across the feasible space. Note, the uniform distribution of the Pareto-optimal solutions on the pump speed-pressure differential panes, which signifies high mutual independence of these variables.

In fig. 9b the Pareto-optimal front of objective vectors and its projections are shown. The Pareto

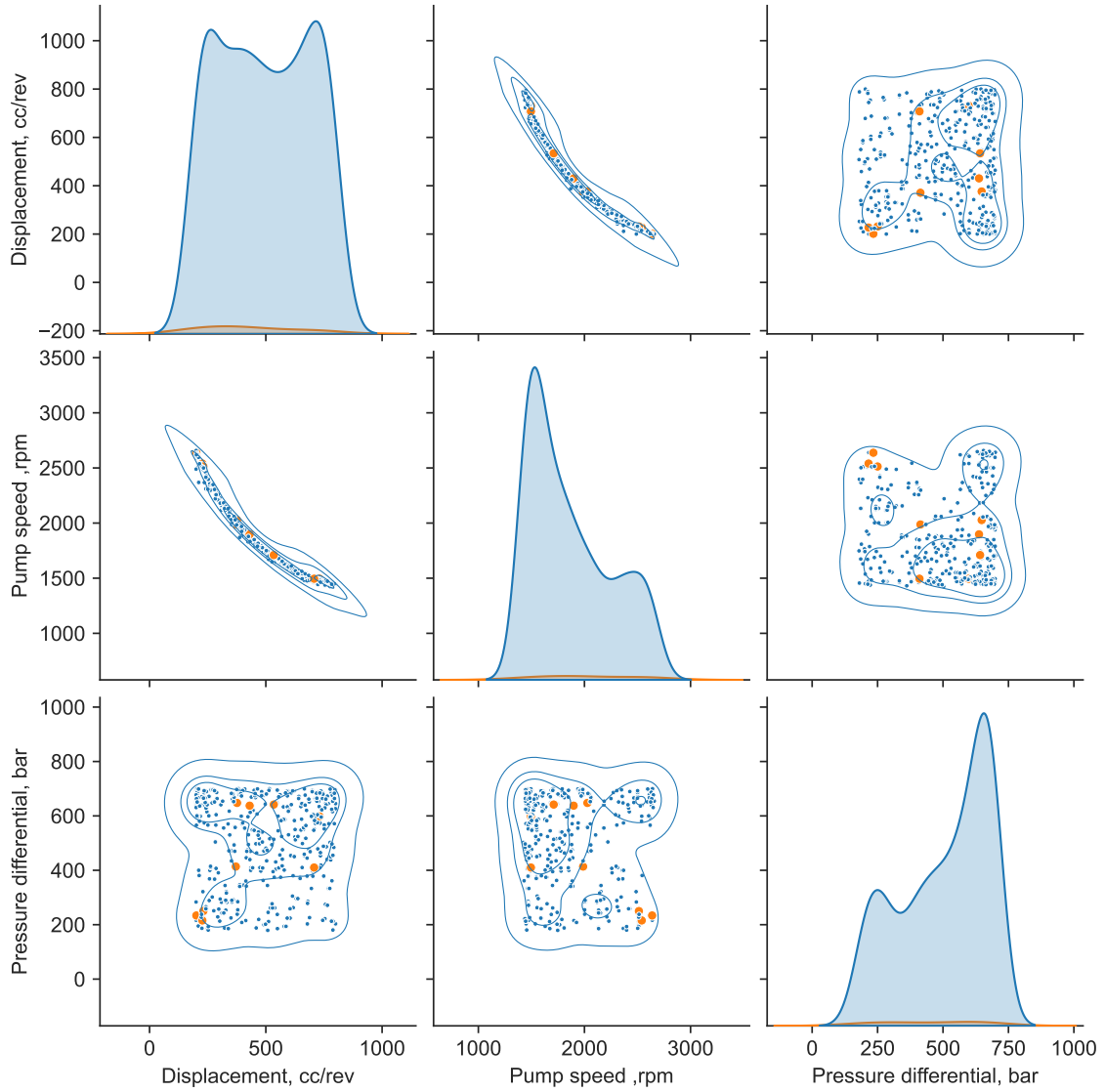


Figure 10: Scattered feasible Pareto-optimal set

frontier takes on a sail-like convex shape in the direction of increasing efficiency and power. High density of high tradeoff solutions can be noted in the high efficiency-low mass corner of the front.

Figures 10 and 11 provide deeper insight into the relative density of the solutions, the vector objective function images distributions. The figures demonstrate plots revealing more dense areas within the non-dominated set and front by plotting the bivariate KDEs. The KDEs on the diagonal

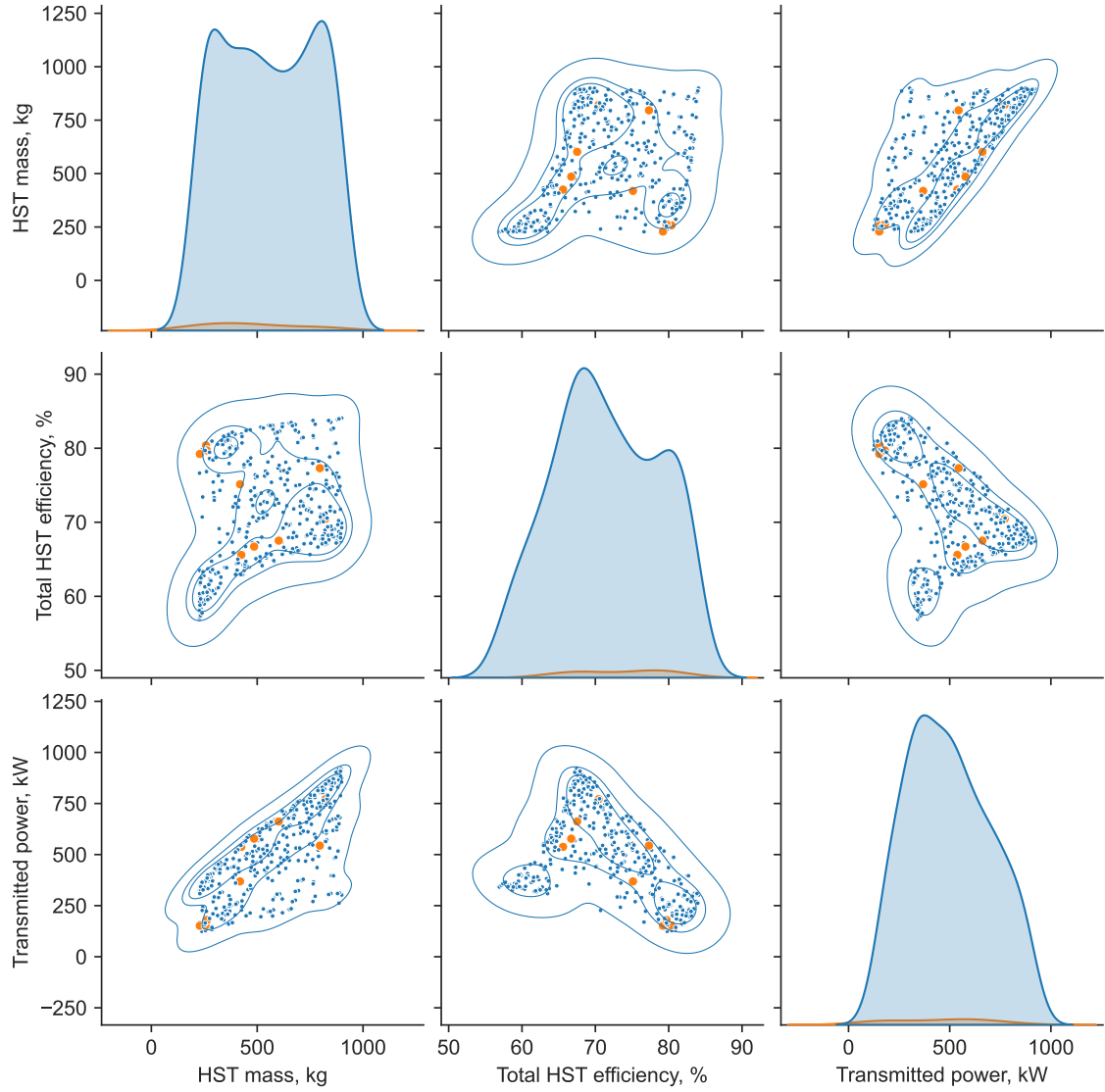


Figure 11: Scattered Pareto-optimal front

highlight the solutions densities, which underline the tendency of the solutions to land on the boundaries or the constraint of the variables. The peaks on the KDE plots on fig. 10 on the diagonal indicate the relative occurrence frequency of various solutions. Figures 10 and 11 emphasize an inclination of the high tradeoff solutions to group the Pareto set corners.

This high-density regions can serve to formulate recommendations to selection of the initial design

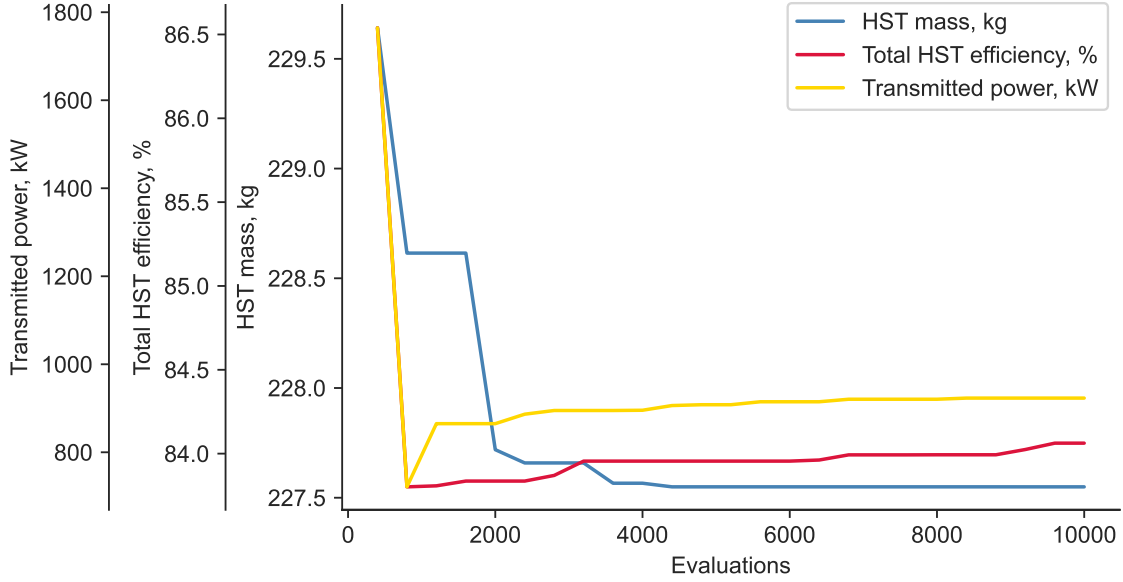


Figure 12: Objectives convergence

546 variables. From the scattered Pareto front on fig. 11 it can be noted that heavier transmissions tend
 547 to be more efficient and transmit more power. There are positive correlations between the power,
 548 efficiency objectives and the HST mass with the power-mass dependence being more pronounced.

549 Analysis of the efficiency model and specifically the contribution of leakages to the power balance
 550 suggests the reason for this observation. It is related to the comparative leakage paths geometry
 551 between the transmissions with different displacements. For the same, constant clearances, the
 552 bigger displacement of the APM would result in wider and longer leakage channel comparing to
 553 smaller displacement machines. Therefore, the actual flow tends to be more laminar in that kind
 554 of channels with less dissipated energy in friction. Hence, according to the employed analytical
 555 efficiency model, the heavier the HST, the more power efficient it is and the more power it transmits.

556 It is noteworthy that with an increase in the transmitted power, the total HST efficiency tend
 557 to decrease. The upper boundary of the Pareto front on the efficiency-power pane plot, see the
 558 third plot in the second column and the second plot in the third column in fig. 11, has a peak at
 559 roughly 85% and 300 kW. The further power increase will cause efficiency decrease to around 67%.
 560 Although, these figure give no direct indication on the HST weight, they are helpful to outline
 561 possible performance limits of the intended transmission on the initial design phases.

562 Since the applied NSGA-II algorithm stores both the non-dominated solutions and objectives, it
 563 is easy to trace back the Pareto-optimal solution from a chosen point on the Pareto-optimal front.

In other words, choosing the desired performance from the non-dominated front on fig. 9b will allow finding the corresponding set of design variables in the non-dominated set on fig. 9a. That would substantially facilitate the decision making in the initial stage of the HST development, i.e. selection the optimal set of the pump displacement, the operating rated speed and the pressure difference between the high- and low-pressure lines of the HST.

Figure 12 shows the convergence of the objectives towards their optimal values from generation to generation. The objectives progress was calculated relative to the number of evaluations, which reaches $n_{gen}M$ evaluations. The figure shows the progress is steady and monotonous converging each objective towards the optimum.

7 Conclusions

The results of the study demonstrated that the multi-objective optimization approach to definition of the initial design variables of HSTs greatly facilitates obtaining, analysis and investigation of the feasible and optimal solutions. This perspective on the conceptual design phase also allows to outline the possible boundaries to and patterns in the performance requirements to the transmission earlier in the design process.

The presented sizing and performance mathematical models of the HST, which were built from two APMs with identical displacements, showed good capability to model and to predict HST performance indicators, i.e. its efficiency, input and output mechanical power parameters. The conducted validation on the large sample of the same size consistently tested HSTs confirmed appropriate accuracy of the volumetric efficiency model.

The example of the efficiency map confirmed the model predictive capability, as the map reflects the expected behaviour of the HST efficiency relative to its operating pump speed and pressure differential. The developed mathematical models have been concluded sufficiently accurate in describing the underlying physical phenomena of power losses in the HST maintaining computational lightness to automate sizing and performance calculations within the optimization algorithm.

The constructed regression models of linear mass and exponential speed limit proved the APM displacement is a good predictor of its speed and mass in a wide range of displacements. The conclusion is supported by the computed models metrics. The quality of the collected data and the built regression models was demonstrated by the high-valued determination coefficients, by sufficiently low root-mean-squared errors and by the evenly distributed model residuals.

Application of NSGA-II driven optimization resulted in the Pareto-optimal set of variables and front of objectives. Algorithm convergence to the optimum was established, demonstrated and discussed. The obtained Pareto-optimal set and front allowed to distinguish regions of the

design space, where the solutions tend to accumulate. Close examination of these regions has facilitated informed decision making, revealing non-trivial relationships between the objectives and design variables, suggesting directions of further design development and attaining tradeoffs between contradicting requirements for an entire power transmission. High tradeoff solutions were identified and analysed. The locations of these solutions in the feasible search space have formed directions of further development in the preliminary and detailed design stages.

References

- Alfredo Arias-Montano, Carlos A. Coello Coello, and Efrén Mezura-Montes. Multiobjective evolutionary algorithms in aeronautical and aerospace engineering. *Trans. Evol. Comp.*, 16(5):662–694, October 2012. ISSN 1089-778X. doi: 10.1109/TEVC.2011.2169968. URL <https://doi.org/10.1109/TEVC.2011.2169968>.
- Katharina Baer, Liselott Ericson, and Petter Krus. Framework for simulation-based simultaneous system optimization for a series hydraulic hybrid vehicle. *International Journal of Fluid Power*, pages 1–13, 2018. doi: 10.1080/14399776.2018.1527122. URL <https://doi.org/10.1080/14399776.2018.1527122>.
- J.M. Bergada, S. Kumar, D.Ll. Davies, and J. Watton. A complete analysis of axial piston pump leakage and output flow ripples. *Applied Mathematical Modelling*, 36(4):1731 – 1751, 2012. ISSN 0307-904X. doi: <https://doi.org/10.1016/j.apm.2011.09.016>. URL <http://www.sciencedirect.com/science/article/pii/S0307904X11005592>.
- Julian Blank and Kalyanmoy Deb. Pymoo: Multi-objective optimization in python. *IEEE Access*, 8: 89497–89509, 2020. doi: 10.1109/ACCESS.2020.2990567.
- MJ Box. A new method of constrained optimization and a comparison with other methods. *The Computer Journal*, 8(1):42–52, 1965.
- Marc Budinger, Jonathan Liscouët, Fabien Hospital, and Jean-Charles Maré. Estimation models for the preliminary design of electromechanical actuators. In *Proceedings of the Institution of Mechanical Engineers, Part G: Journal of Aerospace Engineering*, volume 226, pages 243–259, 2012. doi: 10.1177/0954410011408941. URL <https://doi.org/10.1177/0954410011408941>.
- Marc Budinger, Aurélien Reyssset, Toufic El Halabi, Catalin Vasiliu, and Jean-Charles Maré. Optimal preliminary design of electromechanical actuators. In *Proceedings of the Institution of Mechanical Engineers, Part G: Journal of Aerospace Engineering*, volume 228, pages 1598–1616, 2014. doi: 10.1177/0954410013497171. URL <https://doi.org/10.1177/0954410013497171>.

Qun Chao, Junhui Zhang, Bing Xu, Hsinpu Huang, and Jiang Zhai. Effects of inclined cylinder ports on gaseous cavitation of high-speed electro-hydrostatic actuator pumps: a numerical study. *Engineering Applications of Computational Fluid Mechanics*, 13(1):245–253, 2019. doi: 10.1080/19942060.2019.1576545. URL <https://doi.org/10.1080/19942060.2019.1576545>.

Yuan Chen, Junhui Zhang, Bing Xu, Qun Chao, and Gan Liu. Multi-objective optimization of micron-scale surface textures for the cylinder/valve plate interface in axial piston pumps. *Tribology International*, 2019. ISSN 0301-679X. doi: <https://doi.org/10.1016/j.triboint.2019.06.002>. URL <http://www.sciencedirect.com/science/article/pii/S0301679X19303160>.

Carlos Coello Coello and Maximino Salazar Lechuga. MOPSO: a proposal for multiple objective particle swarm optimization. In *Proceedings of the 2002 Congress on Evolutionary Computation. CEC’02 (Cat. No.02TH8600)*, volume 2, pages 1051–1056 vol.2, May 2002. doi: 10.1109/CEC.2002.1004388.

Selection of Driveline Components. Danfoss Power Solutions, 2015a. BLN-9885.

Pressure and Speed Limits for Hydrostatic Units. Danfoss Power Solutions, 2015b. BLN-9884.

Transmission Circuit Recommendations. Danfoss Power Solutions, 2015c. BLN-9886.

K. Deb, A. Pratap, S. Agarwal, and T. Meyarivan. A fast and elitist multiobjective genetic algorithm: NSGA-II. *IEEE Transactions on Evolutionary Computation*, 6(2):182–197, 2002. doi: 10.1109/4235.996017.

Kalyanmoy Deb. Multi-objective optimisation using evolutionary algorithms: an introduction. In *Multi-objective evolutionary optimisation for product design and manufacturing*, pages 3–34. Springer, 2011.

Kalyanmoy Deb, Karthik Sindhya, and Tatsuya Okabe. Self-adaptive simulated binary crossover for real-parameter optimization. In *Proceedings of the 9th Annual Conference on Genetic and Evolutionary Computation, GECCO ’07*, page 1187–1194, New York, NY, USA, 2007. Association for Computing Machinery. ISBN 9781595936974. doi: 10.1145/1276958.1277190. URL <https://doi.org/10.1145/1276958.1277190>.

J.L. Devore. *Probability and Statistics for Engineering and the Sciences*. Cengage Learning Inc., Boston, MA, 8th edition, 2011.

Andries P Engelbrecht. *Computational intelligence: an introduction*. John Wiley & Sons, 2nd edition, 2007.

- 658 Amine Fraj, Marc Budinger, Toufic El Halabi, Jean charles Mare, and Georgiana-Claudia
659 Negoita. Modelling approaches for the simulation-based preliminary design and optimization of
660 electromechanical and hydraulic actuation systems. In *53rd AIAA/ASME/ASCE/AHS/ASC
661 Structures, Structural Dynamics and Materials Conference*, Honolulu, Hawaii, 2012. doi:
662 10.2514/6.2012-1523. URL <https://arc.aiaa.org/doi/abs/10.2514/6.2012-1523>.
- 663 Daniel Hasko, Lizhi Shang, Eric Noppe, and Emmanuel Lefrançois. Virtual assessment and
664 experimental validation of power loss contributions in swash plate type axial piston pumps.
665 *Energies*, 12(16), 2019. ISSN 1996-1073. doi: 10.3390/en12163096. URL [https://www.mdpi.com/
666 1996-1073/12/16/3096](https://www.mdpi.com/1996-1073/12/16/3096).
- 667 Sun Hui. Multi-objective optimization for hydraulic hybrid vehicle based on adaptive simulated
668 annealing genetic algorithm. *Engineering Applications of Artificial Intelligence*, 23(1):27 – 33,
669 2010. ISSN 0952-1976. doi: <https://doi.org/10.1016/j.engappai.2009.09.005>. URL [http://www.
670 sciencedirect.com/science/article/pii/S0952197609001250](http://www.sciencedirect.com/science/article/pii/S0952197609001250).
- 671 J. D. Hunter. Matplotlib: A 2D graphics environment. *Computing in Science & Engineering*, 9(3):
672 90–95, 2007. doi: 10.1109/MCSE.2007.55.
- 673 Hongchao Jian, Wei Wei, Hongcai Li, and Qingdong Yan. Optimization of a pressure control
674 valve for high power automatic transmission considering stability. *Mechanical Systems and Signal
675 Processing*, 101:182 – 196, 2018. ISSN 0888-3270. doi: <https://doi.org/10.1016/j.ymssp.2017.08.018>.
676 URL <http://www.sciencedirect.com/science/article/pii/S0888327017304466>.
- 677 J. Korn. *Hydrostatic transmission systems*. Intertext Books, 1969. ISBN 9780700200801.
- 678 Petter Krus et al. Simulation based optimisation for system design. In *DS 31: Proceedings of ICED
679 03, the 14th International Conference on Engineering Design, Stockholm*, pages 459–460, 2003.
- 680 L Viktor Larsson. *Control of Hybrid Hydromechanical Transmissions*. PhD thesis, Linköping
681 University Electronic Press, 2019.
- 682 Yunhua Li, Zhanling Ji, Liman Yang, Peng Zhang, Bing Xu, and Junhui Zhang. Thermal-fluid-
683 structure coupling analysis for valve plate friction pair of axial piston pump in electrohydrostatic
684 actuator (EHA) of aircraft. *Applied Mathematical Modelling*, 47:839 – 858, 2017. ISSN 0307-
685 904X. doi: <https://doi.org/10.1016/j.apm.2016.08.015>. URL [http://www.sciencedirect.com/
686 science/article/pii/S0307904X16304395](http://www.sciencedirect.com/science/article/pii/S0307904X16304395).
- 687 Jonathan Liscouët, Marc Budinger, Jean-Charles Maré, and Stéphane Orioux. Modelling approach for
688 the simulation-based preliminary design of power transmissions. *Mechanism and Machine Theory*,

689 46(3):276 – 289, 2011. ISSN 0094-114X. doi: [https://doi.org/10.1016/j.mechmachtheory.2010.11.](https://doi.org/10.1016/j.mechmachtheory.2010.11.010)
690 010. URL <http://www.sciencedirect.com/science/article/pii/S0094114X10002077>.

691 Fangxu Liu, Wei Wu, Jibin Hu, and Shihua Yuan. Design of multi-range hydro-mechanical
692 transmission using modular method. *Mechanical Systems and Signal Processing*, 126:1 –
693 20, 2019. ISSN 0888-3270. doi: <https://doi.org/10.1016/j.ymssp.2019.01.061>. URL <http://www.sciencedirect.com/science/article/pii/S0888327019300445>.

694

695 Alarico Macor and Antonio Rossetti. Optimization of hydro-mechanical power split transmissions.
696 *Mechanism and Machine Theory*, 46(12):1901 – 1919, 2011. ISSN 0094-114X. doi: <https://doi.org/10.1016/j.mechmachtheory.2011.07.007>. URL [http://www.sciencedirect.com/science/](http://www.sciencedirect.com/science/article/pii/S0094114X11001418)
697 [article/pii/S0094114X11001418](http://www.sciencedirect.com/science/article/pii/S0094114X11001418).
698

699 Alarico Macor and Antonio Rossetti. Fuel consumption reduction in urban buses by using power
700 split transmissions. *Energy Conversion and Management*, 71:159–171, 2013. ISSN 0196-8904.
701 doi: <https://doi.org/10.1016/j.enconman.2013.03.019>. URL [https://www.sciencedirect.com/](https://www.sciencedirect.com/science/article/pii/S0196890413001623)
702 [science/article/pii/S0196890413001623](https://www.sciencedirect.com/science/article/pii/S0196890413001623).

703 Noah Manring. *Fluid Power Pumps and Motors: Analysis, Design, and Control*. McGraw-Hill
704 Education, July 2013.

705 Noah D. Manring. Mapping the Efficiency for a Hydrostatic Transmission. *Journal of Dynamic*
706 *Systems, Measurement, and Control*, 138(3), 01 2016. ISSN 0022-0434. doi: 10.1115/1.4032289.
707 URL <https://doi.org/10.1115/1.4032289>. 031004.

708 F. Pedregosa, G. Varoquaux, A. Gramfort, V. Michel, B. Thirion, O. Grisel, M. Blondel,
709 P. Prettenhofer, R. Weiss, V. Dubourg, J. Vanderplas, A. Passos, D. Cournapeau, M. Brucher,
710 M. Perrot, and E. Duchesnay. Scikit-learn: Machine learning in Python. *Journal of Machine*
711 *Learning Research*, 12:2825–2830, 2011.

712 Karl Pettersson. *Design automation of complex hydromechanical transmissions*. PhD thesis,
713 Linköping University Electronic Press, 2013.

714 M. Galal Rabie. *Fluid power engineering*. McGraw-Hill New York, NY, USA, 2009.

715 Lily Rachmawati and Dipti Srinivasan. Multiobjective evolutionary algorithm with controllable
716 focus on the knees of the pareto front. *IEEE Transactions on Evolutionary Computation*, 13(4):
717 810–824, 2009. doi: 10.1109/TEVC.2009.2017515.

718 Antonio Rossetti and Alarico Macor. Multi-objective optimization of hydro-mechanical power split
719 transmissions. *Mechanism and Machine Theory*, 62:112 – 128, 2013. ISSN 0094-114X. doi:

720 <https://doi.org/10.1016/j.mechmachtheory.2012.11.009>. URL <http://www.sciencedirect.com/science/article/pii/S0094114X12002273>.

721

722 Antonio Rossetti and Alarico Macor. Control strategies for a powertrain with hydromechanical
 723 transmission. *Energy Procedia*, 148:978–985, 2018. ISSN 1876-6102. doi: [https://doi.org/](https://doi.org/10.1016/j.egypro.2018.08.064)
 724 [10.1016/j.egypro.2018.08.064](https://doi.org/10.1016/j.egypro.2018.08.064). URL [https://www.sciencedirect.com/science/article/pii/](https://www.sciencedirect.com/science/article/pii/S1876610218303552)
 725 [S1876610218303552](https://www.sciencedirect.com/science/article/pii/S1876610218303552). ATI 2018 - 73rd Conference of the Italian Thermal Machines Engineering
 726 Association.

727 Antonio Rossetti, Alarico Macor, and Martina Scamperle. Optimization of components and layouts
 728 of hydromechanical transmissions. *International Journal of Fluid Power*, 18(2):123–134, 2017. doi:
 729 [10.1080/14399776.2017.1296746](https://doi.org/10.1080/14399776.2017.1296746). URL <https://doi.org/10.1080/14399776.2017.1296746>.

730 Masashi Sasaki, Atsushi Yuge, Toshikazu Hayashi, Hiroshi Nishino, Michiya Uchida, and Toshihide
 731 Noguchi. Large capacity hydrostatic transmission with variable displacement. In *The 9th*
 732 *International Fluid Power Conference*, volume 9, page 25, 2014.

733 Karl Uebel. *Conceptual Design of Complex Hydromechanical Transmissions*. PhD thesis, Linköping
 734 University Electronic Press, 2017.

735 D. Ullman. *The Mechanical Design Process*. McGraw-Hill series in mechanical engineering. McGraw-
 736 Hill Education, 2009. ISBN 9780072975741.

737 Andrea Vacca, Richard Klop, and Monika Ivantysynova. A numerical approach for the evaluation
 738 of the effects of air release and vapour cavitation on effective flow rate of axial piston machines.
 739 *International Journal of Fluid Power*, 11(1):33–45, 2010. doi: [10.1080/14399776.2010.10780996](https://doi.org/10.1080/14399776.2010.10780996).
 740 URL <https://doi.org/10.1080/14399776.2010.10780996>.

741 Alok Vardhan and K. Dasgupta. Mapping the efficiency of the hydrostatic drive for the rotary head
 742 of drill machine using high-speed low-torque hydraulic motors. *Arabian Journal for Science and*
 743 *Engineering*, 43(9):4703–4712, Sep 2018. ISSN 2191-4281. doi: [10.1007/s13369-017-3038-5](https://doi.org/10.1007/s13369-017-3038-5). URL
 744 <https://doi.org/10.1007/s13369-017-3038-5>.

745 Pauli Virtanen, Ralf Gommers, Travis E. Oliphant, Matt Haberland, Tyler Reddy, David Cournapeau,
 746 Evgeni Burovski, Pearu Peterson, Warren Weckesser, Jonathan Bright, Stéfan J. van der Walt,
 747 Matthew Brett, Joshua Wilson, K. Jarrod Millman, Nikolay Mayorov, Andrew R. J. Nelson, Eric
 748 Jones, Robert Kern, Eric Larson, C J Carey, İlhan Polat, Yu Feng, Eric W. Moore, Jake VanderPlas,
 749 Denis Laxalde, Josef Perktold, Robert Cimrman, Ian Henriksen, E. A. Quintero, Charles R. Harris,
 750 Anne M. Archibald, Antônio H. Ribeiro, Fabian Pedregosa, Paul van Mulbregt, and SciPy 1.0

- Contributors. SciPy 1.0: Fundamental Algorithms for Scientific Computing in Python. *Nature Methods*, 17:261–272, 2020. doi: 10.1038/s41592-019-0686-2. URL <https://rdcu.be/b08Wh>.
- Shu Wang. The Analysis of Cavitation Problems in the Axial Piston Pump. *Journal of Fluids Engineering*, 132(7), 07 2010. ISSN 0098-2202. doi: 10.1115/1.4002058. URL <https://doi.org/10.1115/1.4002058>. 074502.
- Michael L. Waskom. seaborn: statistical data visualization. *Journal of Open Source Software*, 6(60): 3021, 2021. doi: 10.21105/joss.03021. URL <https://doi.org/10.21105/joss.03021>.
- F.M. White. *Fluid Mechanics*. McGraw-Hill series in mechanical engineering. McGraw Hill, 2011. ISBN 9780073529349.
- Shuai Wu, Bo Yu, Zongxia Jiao, Yaoxing Shang, and PCK Luk. Preliminary design and multi-objective optimization of electro-hydrostatic actuator. *Proceedings of the Institution of Mechanical Engineers, Part G: Journal of Aerospace Engineering*, 231(7):1258–1268, 2017. doi: 10.1177/0954410016654181. URL <https://doi.org/10.1177/0954410016654181>.
- Bing Xu, Min Hu, Jun-hui Zhang, and Qi Su. Characteristics of volumetric losses and efficiency of axial piston pump with respect to displacement conditions. *Journal of Zhejiang University-SCIENCE A*, 17(3):186–201, Feb 2016. doi: 10.1631/jzus.A1500197. URL <https://doi.org/10.1631/jzus.A1500197>.
- Longxian Xue, Shuai Wu, Yuanzhi Xu, and Dongli Ma. A simulation-based multi-objective optimization design method for pump-driven electro-hydrostatic actuators. *Processes*, 7(5), 2019. ISSN 2227-9717. doi: 10.3390/pr7050274. URL <https://www.mdpi.com/2227-9717/7/5/274>.
- Bo Yu, Shuai Wu, Zongxia Jiao, and Yaoxing Shang. Multi-objective optimization design of an electrohydrostatic actuator based on a particle swarm optimization algorithm and an analytic hierarchy process. *Energies*, 11(9), 2018. ISSN 1996-1073. doi: 10.3390/en11092426. URL <https://www.mdpi.com/1996-1073/11/9/2426>.
- Chi Zhang, Xu Han, Tatiana Minav, and Yongling Fu. Multi-objective optimization design of a 30 kw electro-hydrostatic actuator. *Proceedings*, 64(1), 2020. ISSN 2504-3900. doi: 10.3390/IeCAT2020-08525. URL <https://www.mdpi.com/2504-3900/64/1/5>.
- Junhui Zhang, Qun Chao, Qiannan Wang, Bing Xu, Yuan Chen, and Ying Li. Experimental investigations of the slipper spin in an axial piston pump. *Measurement*, 102:112 – 120, 2017. ISSN 0263-2241. doi: <https://doi.org/10.1016/j.measurement.2017.01.035>. URL <http://www.sciencedirect.com/science/article/pii/S0263224117300453>.

782 Aimin Zhou, Bo-Yang Qu, Hui Li, Shi-Zheng Zhao, Ponnuthurai Nagaratnam Suganthan,
783 and Qingfu Zhang. Multiobjective evolutionary algorithms: A survey of the state of the
784 art. *Swarm and Evolutionary Computation*, 1(1):32 – 49, 2011. ISSN 2210-6502. doi:
785 <https://doi.org/10.1016/j.swevo.2011.03.001>. URL [http://www.sciencedirect.com/science/](http://www.sciencedirect.com/science/article/pii/S2210650211000058)
786 [article/pii/S2210650211000058](http://www.sciencedirect.com/science/article/pii/S2210650211000058).